LANGMUIR

pubs.acs.org/Langmuir Article

# The Relation between Colloid Size and Nanoscale Water Transport Pathways in Waterborne Acrylic Coatings as Seen by Small-Angle Neutron Scattering

Riccardo Biella,* Lakshmi Satish Nair, Steven R. Parnell, A. Catarina C. Esteves, Chintankumar Patel, Patrick Keil, and Santiago J. Garcia*

Cite This: *Langmuir* 2026, 42, 10205−10222 Read Online

ACCESS | Metrics & More | Article Recommendations | Supporting Information

**ABSTRACT:** Waterborne and water-reduced coatings are increasing in relevance in many sectors as an alternative to solventborne coatings. In this work, the internal structure of waterborne polymers as a function of colloid particle size is unveiled and directly related to macroscopic water absorption. To this aim, a set of acrylic waterborne films was prepared from dispersions of different colloidal particle sizes (100, 150, and 200 nm) with the same surfactant coverage. Macroscopic water absorption and water affinity were studied by Dynamic vapor sorption (DVS) and immersion tests. Small-Angle Neutron Scattering (SANS) was used to study deuterated water diffusion with time. This revealed the presence of remnant hydrophilic colloid−colloid interphases in all films, independently of the forming colloidal size and annealing conditions. Moreover, fitting of SANS data revealed that water transport in these films happens through surfactant-rich colloid−colloid interphases or through 10 nm-wide hydrophilic paths rich in surfactant aggregates (in the range of 4 nm) when these are present. The presence of the hydrophilic paths explains the higher water uptake measured in waterborne films made from 100 nm colloids, a process so far not previously reported. This study highlights how water diffusion in waterborne films may be engineered through fine control of particle size and film formation conditions.

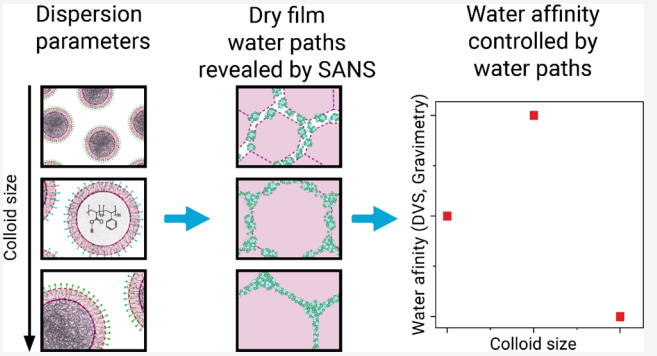




## INTRODUCTION

The interest in waterborne and water-reduced coatings with reduced volatile organic compound (VOC) emissions is continuously growing due to increasing sustainability and environmental restrictions and the increasing performance of this coating family.[1] One of the most challenging applications of waterborne coatings is in the field of anticorrosion coatings for infrastructure and transport; a crucial application domain due to the growing costs and environmental impact related to corrosion and degradation of infrastructure.[2] Despite the current understanding of film formation from waterborne polymeric colloidal suspensions,[1] further developments in the field will benefit from a deeper understanding of the relationship between the colloidal system parameters, the structure of nanoheterogeneities, and the macroscopic properties. In this context, the absorption and transport of water in the coating are highly relevant to the anticorrosion performance.[3−5]

To explain the correlation between water absorption, electrochemical properties, and the anticorrosion performance of the coating, various physical models,[6,7] finite element studies,[8] and, more recently, machine learning models[9] have also been proposed. The downside of electrochemical or gravimetric techniques is that they are bulk techniques, which average over the whole coating, while water transport and the anticorrosion performance depend on the local structure of the material. Recent reports using Fourier-Transform Infrared Spectroscopy (FTIR) coupled with Atomic Force probes (AFM)[10,11] highlighted the highly heterogeneous water uptake in solventborne epoxy coatings, with water uptake following nanoscale heterogeneities created during the curing process.[10] A larger understanding of the role of local nanoscale heterogeneities and pathways on water transport appears as a key aspect to increase the anticorrosion performance of organic coatings.

Unlike solventborne coatings, waterborne coatings are formed out of water dispersions of solid polymeric nanoparticles (i.e., polymeric binder), often accompanied by organic species such as surfactants and inorganic additives such as corrosion

Received: October 29, 2025
Revised: February 12, 2026
Accepted: February 12, 2026
Published: April 8, 2026





https://doi.org/10.1021/acs.langmuir.5c05519
*Langmuir* 2026, 42, 10205−10222

Table 1. Waterborne Dispersion Parameters[a]

| dispersion name | average particle size by DLS (nm) | surfactant concentration (phr) | surfactant surface coverage (%) | solid content (%) | $M_w$ (kDa) | pH |
|---|---|---|---|---|---|---|
| WB100 | 102 ± 1 | 2 | 44 ± 5 | 47.1 | 140 ± 20 | 8.5 |
| WB150 | 156 ± 1 | 1 | 44 ± 5 | 49.7 | 140 ± 20 | 8.5 |
| WB200 | 198 ± 1 | 0.85 | 44 ± 5 | 52.8 | 140 ± 20 | 8.5 |

[a]phr in column 3 stands for "parts per hundred resin", e.g., 2 g of surfactant was used for each 100 g of polymer.

inhibitors, fillers, and/or pigments. When dealing with the polymeric binder alone, the film-forming process involves (i) the packing and deformation of the nanoparticles during water (and cosolvent) evaporation and (ii) the organization of surfactant adsorbed on the nanoparticles or/and dissolved in water.[12−14] During this process, the nanoparticles locally soften and deform to fill the voids created during imperfect packing, in a process that is highly sensitive to the dispersion properties and drying conditions. Following deformation, polymer chains interdiffuse across the nanoparticle interfaces, resulting in polymers that are homogeneous at the macroscale but retain heterogeneity at the nanoscale.

The nanostructure of waterborne films is generally studied by Scanning/Transmission Electron Microscopy (SEM/TEM) or Atomic Force Microscopy (AFM). Electron Microscopy has been successfully used to image particle packing and deformation in waterborne coatings from suspensions with different chemical compositions,[15] under different film formation temperatures[16] and for different particle stiffnesses.[17,18] Similarly, AFM has been used to study the effect of film formation temperature (FFT),[19] the addition of ionic[20] and polymeric[21,22] surfactants, lateral drying inhomogeneities,[23] and modulus of the latex particles.[24,25] These studies revealed that full particle coalescence (i.e., apparent disappearance of the colloid−colloid interfaces) can be achieved in latexes with sufficiently low glass transition temperature and polymer stiffness.[17]

Recent studies using Small-Angle X-ray Scattering (SAXS),[26] Grazing Incidence Ultrasmall Small-Angle X-ray Scattering (GIUSAXS),[24] and Scanning Electric Potential Microscopy (SEPM)[27] have nevertheless highlighted that, even latexes that appear smooth and fully coalesced according to AFM or SEM analysis, retain nanoscale colloid−colloid interphases. Seemingly, these interphases have a different electron density than the cores of the latex particles and a different electrical potential. Surfactant accumulation[26,27] and incomplete chain interdiffusion[28] have been proposed as possible reasons for the presence of these colloid−colloid interphases.

Small-angle scattering techniques using neutrons (SANS) or X-rays (SAXS) are particularly powerful to study the nanoscale structure of waterborne films due to their sensitivity in the 1−1000 nm range. In these techniques, the neutron or X-ray beam is directed toward the sample placed at a predefined distance from a detector positioned behind the sample. The detector collects the angles at which the neutrons or X-rays are scattered when passing through the sample. The resulting scattering intensity pattern contains information about the presence, size, and shape of scattering sites in the material. As a volumetric technique, the signal can, therefore, be related to the presence of repeated nanostructures in the material.

SAXS has been recently used to study waterborne latexes using films dried in situ in very specific conditions,[24,26,29,30] which is however expected to severely affect the resulting polymer nanostructure[19] and complicate the extrapolation of the results to more realistic polymer films. SANS has been used with deuterated compounds to highlight targeted features within the material.[31] Following this principle, deuterated water ($D_2O$),[32,33] deuterated polystyrene,[34,35] or deuterated polar and apolar solvents[33] have been used to identify the presence of hydrophilic interphases[32,33] and hydrophobic cores[33−35] in dry latex films using a qualitative analysis of the SANS peaks. More sophisticated methods relying of the fitting of physical models have been used on wet latexes[36,37] and only recently on a dried latex with a deuterated surfactant,[38] but some fine-tuning is required and such approaches have, so far, failed to fully describe waterborne polymer films. Moreover, the actual water transport pathways have not yet been investigated.

In this work, we used SANS, DVS, and gravimetry tests to study the relation between colloid particle size, dry film nanostructure, and the resulting macroscopic water absorption mechanisms. We used an industrially relevant, model acrylic colloidal dispersions with different colloid particle sizes but constant chemical composition, molecular weight, pH, surfactant coverage, and surface charge density. The resulting water pathway nanostructure shows a clear dependence on the colloid size, influencing in turn the macroscopic water uptake properties.

## MATERIALS AND METHODS

### Sample Preparation

Waterborne dispersions were provided by BASF SE. These were produced by emulsion polymerization by copolymerizing 49 parts by weight butyl acrylate, 49 parts by weight styrene, and 2 parts by weight methacrylic acid using ammonium persulfate as initiator. After the emulsion polymerization, the pH was brought to 8.5 by the addition of ammonia solution (25%). Sodium salt of alkyl ether sulfate was used as a surfactant. The amount of surfactant concentration used in each dispersion was varied to achieve almost similar surface coverage (∼44%) of the colloids in all dispersions. The important characteristic parameters of the dispersions used in this study are shown in Table 1.

Before film casting, the dispersions as provided by BASF were diluted with 50% in weight distilled water to facilitate casting, and 3 phr butylglycol (Thermo Fisher Scientific) was added as a coalescing aid. The water-diluted dispersions were mixed at 2000 rpm for 5 min using a SpeedMixer DAC 400.2 VAC-P. Four milliliters of the dispersions were then cast on a 60 mm glass Petri dish with a syringe and left to dry at 22 °C and 38% RH for 1 week. Some films produced with the WB100 and WB200 dispersions were further annealed in an oven at 50 or 80 °C for 1 day. The resulting films were approximately 450 $\mu$m thick and were directly peeled off of the Petri dish using a spatula. The dry films were kept in a desiccator prior to testing. Characteristic film properties were measured and are summarized in Table 2.

### SANS Measurements

Small-angle neutron scattering (SANS) measurements were performed at the LARMOR instrument at the ISIS facility in the UK, using a sample-to-detector distance of approximately 4 m, with the beam dimensions 6 × 8 mm centered on the 2-D detector. A Q range of 0.005−0.7 $Å^{-1}$ was obtained using a wavelength range of 0.9−13.3 Å. Polymer film rectangles measuring 20 × 9 mm, cut with scissors, were immersed in $D_2O$ (Sigma-Aldrich) for 2, 6, 12, and 48 h prior to measurements and then patted dry to remove excess $D_2O$ and inserted in 1 mm path length quartz cuvettes (Starna) and sealed with a PTFE


https://doi.org/10.1021/acs.langmuir.5c05519
Langmuir 2026, 42, 10205−10222

**Table 2. Characteristic Film Properties for the Tested Films**

| film name | annealing temperature (°C) | particle size DLS (nm) | dry film thickness (mm) |
|---|---|---|---|
| WB100-RT | (−) | 102 ± 1 | 0.45 ± 0.02 |
| WB150-RT | (−) | 156 ± 1 | 0.43 ± 0.06 |
| WB200-RT | (−) | 198 ± 1 | 0.49 ± 0.03 |
| WB100-50C | 50 | 102 ± 1 | 0.62 ± 0.03 |
| WB100-80C | 80 | 102 ± 1 | 0.43 ± 0.05 |
| WB200-50C | 50 | 198 ± 1 | 0.49 ± 0.03 |
| WB200-80C | 80 | 198 ± 1 | 0.36 ± 0.06 |

cap and parafilm to minimize water desorption and D/H exchange during the 50 min duration measurements. The cells were washed with ultrapure water and acetone between tests. Utmost care was taken to time the immersion of the samples to minimize the time the sample spent in the sealed cuvette, with a particular focus on samples measured forshort immersion times.

The measurement time was ∼5 min for transmission spectra and ∼40 min for SANS, for a total of ∼50 min for each sample. The 2D scattering intensity was radially averaged to obtain the scattering intensity as a function of the scattering vector magnitude $q$, following the data reduction procedure presented in the literature.[31] The data was reduced in Mantid with the SANS Reduction algorithm. The empty beam, empty quartz cuvette, and a standard polymer sample were used to calibrate the beam and correct for the cuvette scatter. Multiple scattering was checked by superimposing scattering curves of neutrons of different wavelength bands. The data was fitted in SASView 5.0.6. In small particle size films, the domain was split around $q = 0.4$ Å$^{-1}$ to fit the different parts of the model to ensure a proper fit. The parameters were constrained to physical values. Different fitting models were used, as discussed in the results section.

### Dynamic Vapor Sorption Measurements

DVS measurements were conducted on a Surface Measurement Systems DVS Resolution. A free-standing polymer film (12 mm discs, ∼40 mg) was placed inside the sample pan, ensuring exposure to water vapor from both sides. The temperature was fixed at 25 °C during the complete measurement. The sample was first equilibrated and dried by setting the RH to zero for 4 h. Next, the RH was increased in steps of 10% from 0% RH to 90% RH with a final step at 95% RH. Lowering of the RH was done in a reverse manner. The RH was kept constant until the $dm/dt$ was less than 0.001 or for a maximum of 6 h. This ensured that the final mass uptake corresponded to the quasi-equilibrium value. The data was fitted in Origin 2025 using the Levenberg−Marquardt algorithm.

### Gravimetric Water Absorption Measurements

Gravimetric water absorption experiments were carried out for 2 days to measure the water absorption rate. To this aim, 20 mm diameter circular samples (approximately 150 mg) were immersed in 30 mL of deionized water. Before each weighing, each sample was slightly tapped with absorbent paper to remove excess water on the surface. The samples were weighed using a standard laboratory scale with a precision of ±0.1 mg.

## RESULTS AND DISCUSSION

### Gravimetric Water Absorption Measurements

Gravimetric water absorption was performed to measure the macroscopic water uptake. Figure 1 shows the results of gravimetric water absorption measurements. The samples absorb between ∼6 wt % (WB200-RT) and ∼10 wt % (WB150-RT) of water in the 48 h immersion time used in this work (Figure 1a). At lower immersion times (∼2 h), there is no statistical difference between the WB100-RT and WB200-RT samples, with the WB150-RT sample exhibiting slightly higher water absorption. A clear difference between all the samples starts appearing from 6 h, only to become more evident after 24 h of immersion. The water uptake kinetics after 6 h appears to be dependent on the particle size, with faster water uptake for the WB150-RT sample and the lowest for the WB200-RT sample. As will be discussed in the DVS and SANS analysis, this can be attributed to differences in the film forming as a function of the colloid size. As can be seen in Figure 1b, the scatter for the intermediate colloid particle size WB150-RT sample is the highest while maintaining the highest water uptake. This behavior points at a larger architectural heterogeneity for the midrange particle size films, independently of the film casting and region of the film tested.

### Dynamic Vapor Sorption Measurements

Gravimetric experiments provide insight into the macroscopic trends in water absorption. Dynamic vapor sorption measurements were performed to gain a more detailed understanding of the underlying mechanisms. In this method, the sample is exposed to increasing RH levels, reaching a quasi-equilibrium at each step between the water adsorbed and absorbed by the sample and the ambient humidity. Figure 2 shows the curve detailing the quasi-equilibrium water uptake at each RH level, defining the film sorption isotherm. It should be noted that for

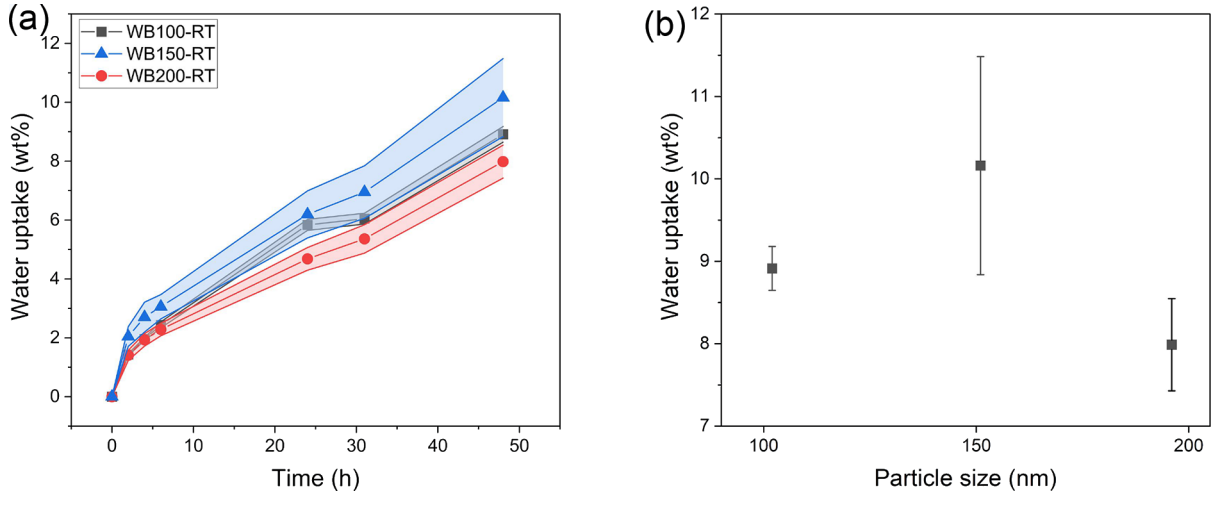


**Figure 1.** Gravimetric water absorption results. (a) Water uptake in % as a function of time and (b) water uptake after 48 h of immersion.



https://doi.org/10.1021/acs.langmuir.5c05519
Langmuir 2026, 42, 10205−10222

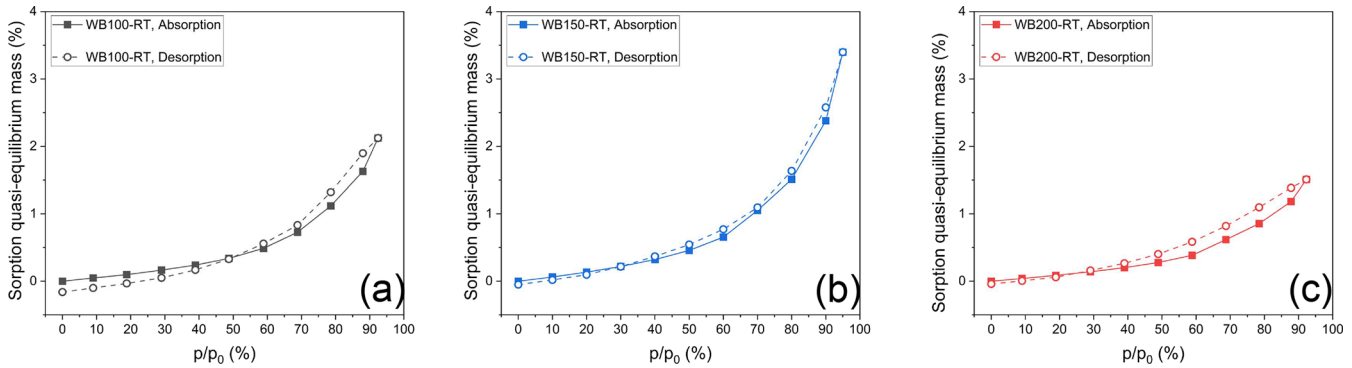


**Figure 2.** Water sorption and desorption isotherms measured by DVS for samples (a) WB100-RT, (b) WB150-RT, and (c) WB200-RT. Sorption mass is measured after 4 h of vapor exposure.

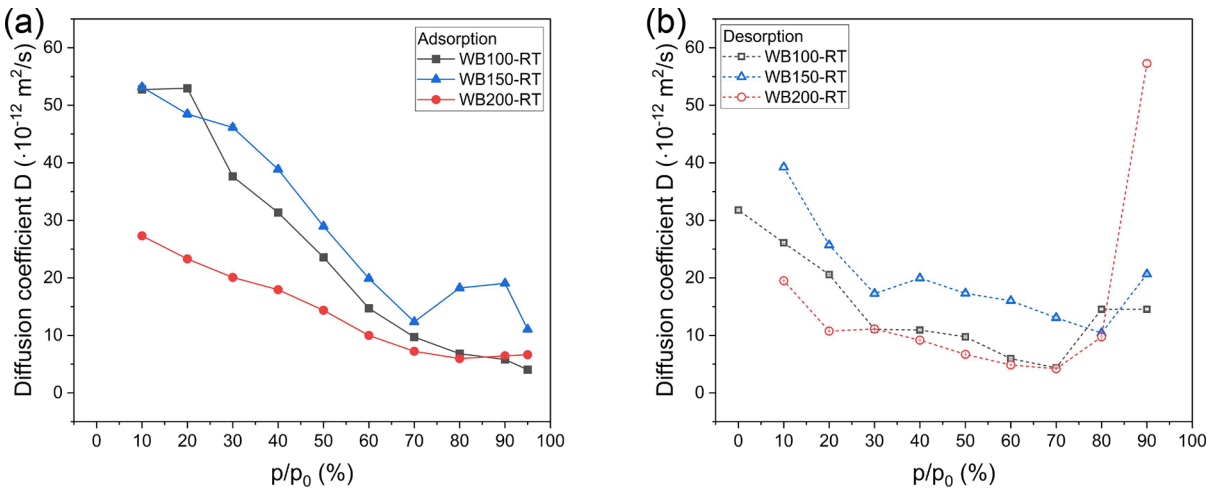


**Figure 3.** Cumulative diffusion coefficients for (a) adsorption and (b) desorption cycles. Note: the diffusion coefficient $D$ for sample WB200-RT at 95% $p/p_0$ is related to a fitting artifact due to the behavior of the polymer being further from Fickian behavior.

higher RH % (RH ≥ 70%), the samples are not at full equilibrium water sorption (Figure S1), and the reported DVS values are likely a slight underestimation of the actual sorption mass.

As shown in Figure 2, at relative humidities ≤40% RH, the sorption isotherms of all samples show a linear behavior consistent with Henry's law, which describes ideal gas−liquid dissolution.[39] Under these conditions and in agreement with the gravimetry results (Figure 1), the medium particle size sample shows the highest affinity for water (WB150-RT, Figure 2b) as evidenced by the higher quasi-equilibrium water uptake compared to the sample with larger particles (WB200-RT, Figure 2c) and that with the smallest particle size (WB100-RT, Figure 2a). At higher relative humidities (RH >50%), water uptake deviates from ideal linear behavior and increases exponentially for all samples. This effect is generally attributed to the clustering of water molecules at pores or hydrophilic sites and hydroplasticization (i.e., the increase in polymer chain mobility induced by water molecules), as reported elsewhere.[40] At these high RHs, it becomes more evident that the medium particle size polymer film absorbs more water than the polymer films created with either the largest or the smallest particle sizes, indicating a greater influence of water clustering and hydroplasticization effects.

The desorption curve exhibits some degree of hysteresis with a higher quasi-equilibrium moisture content during the desorption phase compared to the adsorption phase. This is especially evident at higher relative humidities. Hysteresis has been previously reported in waterborne acrylic resins[41] and porous acrylic polymers.[42] Although swelling has been proposed as a possible hysteresis mechanism,[42] more experimental evidence is needed to fully explain and characterize this phenomenon. The other notable feature of the desorption curve is the final negative value in desorption, which is especially pronounced for the WB100-RT sample and has been recently reported for other acrylic films.[41] This negative value suggests additional desorption of lighter chemical species trapped within the polymer matrix during film formation, such as the cosolvent, surfactant, or unreacted monomers. It is argued that irreversible changes in the polymer structure and hydroplasticization enable the migration of these chemical species to the surface during the desorption process.

Despite the expected non-Fickian nature of water diffusion through the polymers under study, Fick's diffusion law was found to fit each relative humidity interval (i.e., every 10% RH steps) reasonably well (Figure S1), except for the last RH % step (RH = 95%) where the behavior of the polymer is further from Fickian. The solution to Fick's diffusion law takes the form (eq 1):[41]

$$M_t = M_{initial} + (M_{final} - M_{initial}) \left(1 - \sum_{i=0}^{\infty} \frac{8}{(2n+1)\pi^2} \exp \frac{-D(2n+1)^2\pi^2 t}{4 \times l^2}\right) \quad (1)$$



https://doi.org/10.1021/acs.langmuir.5c05519
Langmuir 2026, 42, 10205−10222

where $M_{initial}$ and $M_{final}$ are the starting and final mass, respectively, $t$ is the time, $l$ is the film thickness, and $D$ is the calculated water diffusion coefficient in the polymer. $D$ is then plotted in Figure 3 for the adsorption (Figure 3a) and desorption (Figure 3b) results. In this context, the diffusion coefficient represents the diffusivity of water in the polymer matrix created at a specific relative humidity. The diffusion coefficient decreases with increasing RH; at low RH, the free volume allows faster water transport, while at higher RH, a certain degree of rearrangement in the polymer chains is needed to allow water ingress. This is in agreement with other reports using waterborne acrylic films.[40,41] The cumulative diffusion coefficients exhibit the same trend as the sorption isotherm, confirming the higher affinity for water in the medium particle size WB150-RT samples. Moreover, the diffusion coefficients of the WB200-RT samples appear to vary less with the relative humidity than those of the WB100-RT or WB150-RT samples. As will be discussed further on, we attribute this behavior to the different water transport pathways revealed by SANS.

To get further insights into the water absorption behavior of the polymers, the sorption isotherms were fitted using the Brunauer–Emmett–Teller (BET) theory model, the Guggenheim–Anderson–de Boer (GAB) model, and the ENSIC model. A detailed description of the models and a comparison of their fitting quality can be found in Figures S2 and S3. The most useful fit was obtained with a combination of the BET[43] model for RH ≤ 60% and ENSIC[44,45] model for the region above 60%RH, as explained in the Supporting Information in detail and seen in Figure 4.

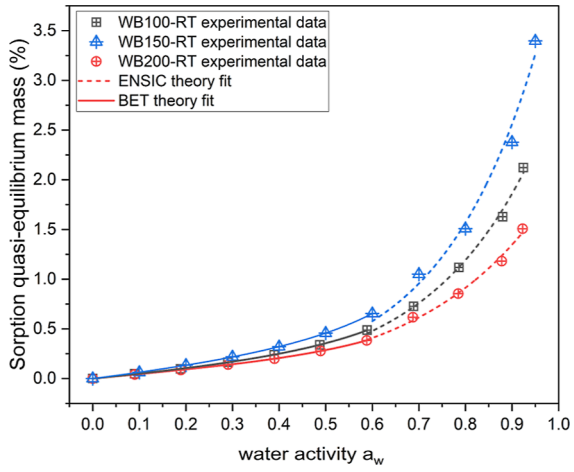


**Figure 4.** Fitting result of the sorption isotherms using a combined BET/ENSIC model overlapping at $a_w = 0.6$. Straight line: BET model fit, dashed line: ENSIC model fit.

The final model used to fit the curves, shown in Figure 4 as solid (BET) and dashed (ENSIC) lines, can be described by eq 2:

$$M_{equilibrium} = \begin{cases} \dfrac{m_m C_{BET} a_w}{(1 - a_w)(1 + (C_{BET} - 1)a_w)}, & a_w \leq 0.6 \\ \dfrac{\exp((k_s - k_p)a_w) - 1}{(k_s - k_p)/k_p}, & a_w > 0.6 \end{cases} \quad (2)$$

where $a_w$ is the water activity (equal to the partial pressure); $m_m$ is the monolayer water capacity ($g_{H_2O}/m^3$); $C_{BET}$ is a fitting constant related to the difference in energy of adsorption to the polymer and energy of liquefaction (see Supporting Information for more details), and $k_s$ and $k_p$ are interaction parameters similar to the interaction parameter from the Flory–Huggins theory.[44,45] The relevant characteristic parameters resulting from the fitting process can be seen in Figure 5 and Table S1.

The higher monolayer water capacity (Figure 5a) of the samples WB100-RT and WB150-RT compared to the WB200-RT sample indicates a higher amount of readily available sites for water adsorption for the mid and small colloid sizes. Moreover, the same samples showcase a lower $C_{BET}$ constant (Figure 5b). In line with the higher monolayer water capacity, this indicates water absorption is favored in the low and mid colloidal range samples due to the lower energy barrier associated with water adsorption. Both results explain the higher water uptake at lower relative humidities for WB100-RT and WB150-RT samples (Figure 4).

The ENSIC model for the high-RH area of the graph yields similar water–polymer affinity parameters among the three systems (Figure 5c). In this context, we relate the water–polymer affinity parameter to the interaction of water with the average polymer and surfactant molecules. The similar chemistry of the samples can explain this result. The water–water affinity parameter is lowest for the WB200-RT sample and highest for the WB150-RT sample (Figure 5d). A rigorous physical interpretation of this parameter is not straightforward, especially in a ternary system with surfactant, polymer, and water; nevertheless, this result can be qualitatively interpreted as a lower tendency of water to form clusters in the case of the films made from 200 nm colloids. This in turn is reflected in the lower sorbed water at high relative humidities for 200 nm colloids (Figure 4).

## SANS Data and Selection of a Physically Representative Fitting Model

Small-Angle Neutron Scattering (SANS) measurements were performed to characterize the nanostructure of water within the material. Figure 6 shows the scattering cross-section (or intensity) $I$ as a function of the scattering vector $q$ of all of the studied polymers at different immersion times in water. As such, an $I = f(q)$ plot gives an indication of how strongly a sample scatters neutrons ($I$) as a function of the change in the direction between the incoming and scattered neutron ($q$), which corresponds to the spatial resolution being probed (i.e., the dimension of the repeated feature that scatters neutrons). The scattering cross-section can be conceptualized as an interference pattern that contains information about characteristic repeating patterns in the material. Peaks in the scattering intensity can be related to repeating characteristic distances through the equation $d_{characteristic} = 2\pi/q$. This means that low-$q$ features correspond to large physical features and vice versa. It should finally be noted that all the values obtained correspond to the response of the whole film thickness and can therefore be considered as thickness-averaged.

To retrieve quantitative shape and size information on the coating's physical features present in the scattering intensity functions (i.e., how water is present in determined features within the film), physical models can be used to fit the data. During the model selection process, it was found that no individual model reported in the literature yielded a sufficiently good fit for any of our data sets, which can be attributed to the


https://doi.org/10.1021/acs.langmuir.5c05519
Langmuir 2026, 42, 10205−10222

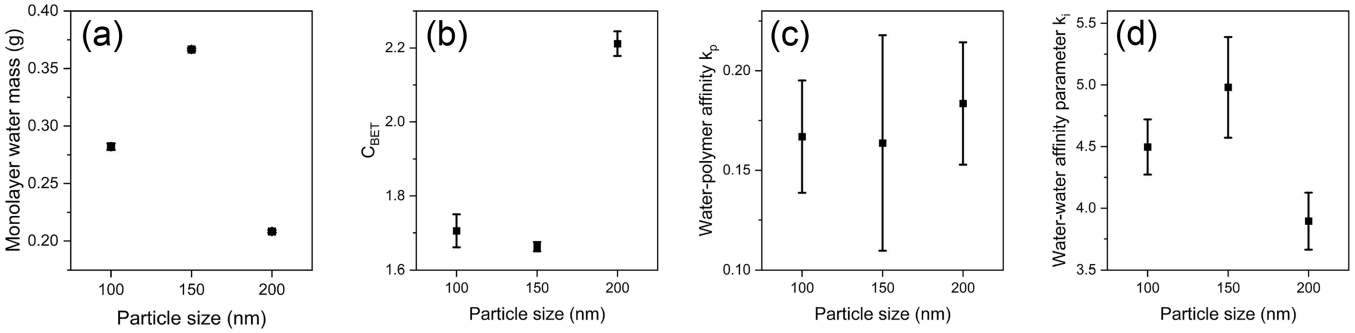


**Figure 5.** Results of the combined BET/ENSIC model for the room-temperature samples (−RT). (a) Monolayer water mass mm (error bars are within the size of the plotted points), (b) $C_{BET}$ from the BET model, (c) water−polymer affinity parameter $k_p$, and (d) water−water affinity parameter $k_i$ from the ENSIC model at higher RHs.

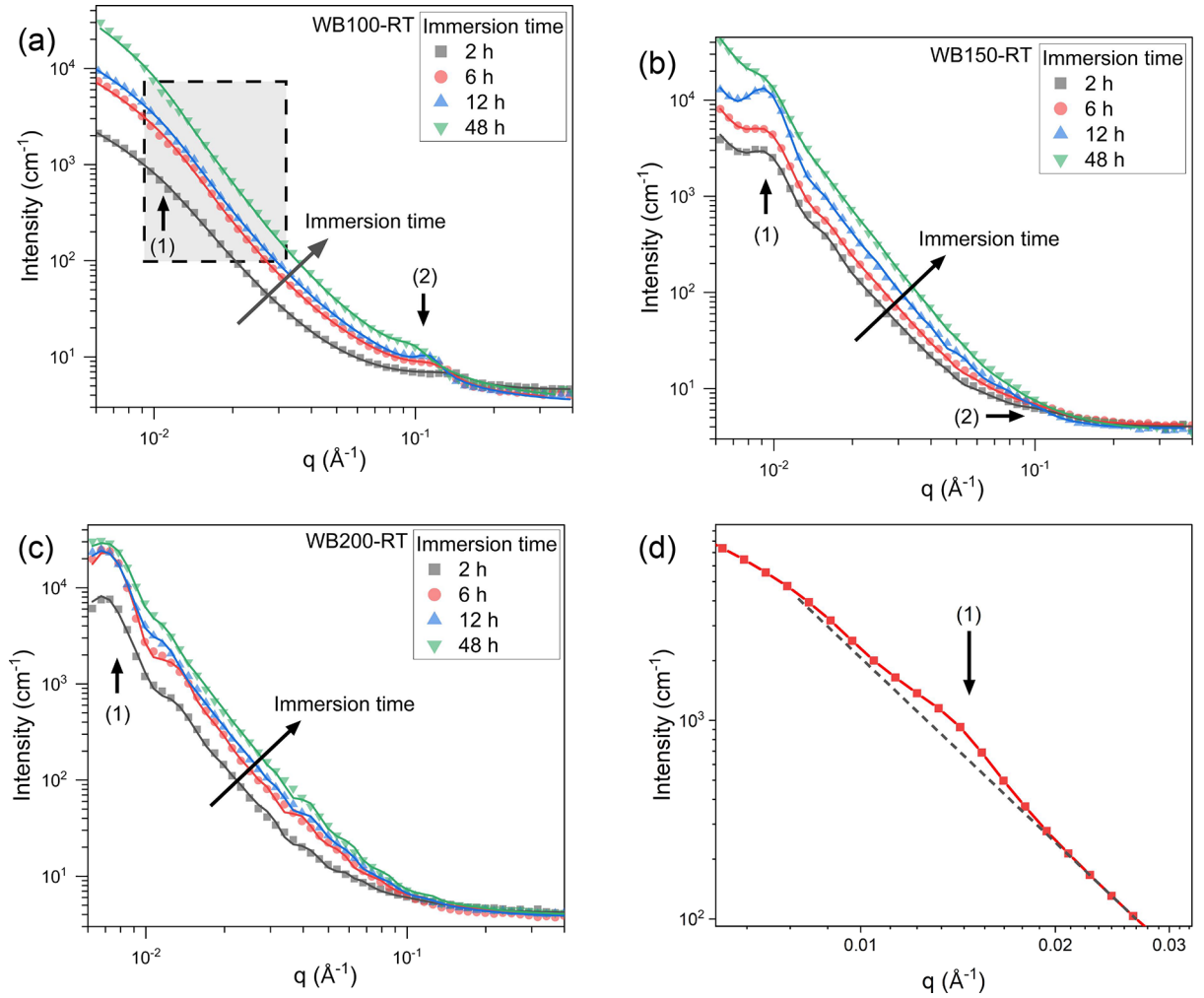


**Figure 6.** Neutron scattering results for waterborne, room-temperature-casted samples. The solid lines showcase the fits to the model finally selected in this work. (a) WB100-RT shows a bigger feature (1), associated with water paths, and small feature (2), which can be attributed to surfactant aggregates; (b) WB150-RT, highlights the colloid interphase (1) as well as a similar small feature (2) as for the WB100-RT samples; (c) WB200-RT shows a clear colloid−colloid interphase (1); and (d) zoom of WB100-RT at 6 h immersion time in the low-$q$ region, where a deviation from the Porod behavior is highlighted. The dashed line in subfigure d guides the eye with an ideal Porod behavior.

complex structure of the water transport pathways in our samples. To overcome this challenge, a composite model with two to three individual components capturing separate contributions to the measured scattering intensity was employed following a recently reported strategy.[46] The resulting fitting curves are shown in Figure 6 overlapped with the experimental data, and the model selection process is discussed subsequently.

The WB150-RT and WB200-RT samples exhibit clear sharp peaks (peak (1) in Figure 6b,c) in the low $q$ region indicative of a regular, spatially repeating structure. Similar peaks have been reported in the literature for other waterborne films[33,34] and


https://doi.org/10.1021/acs.langmuir.5c05519
Langmuir 2026, 42, 10205−10222

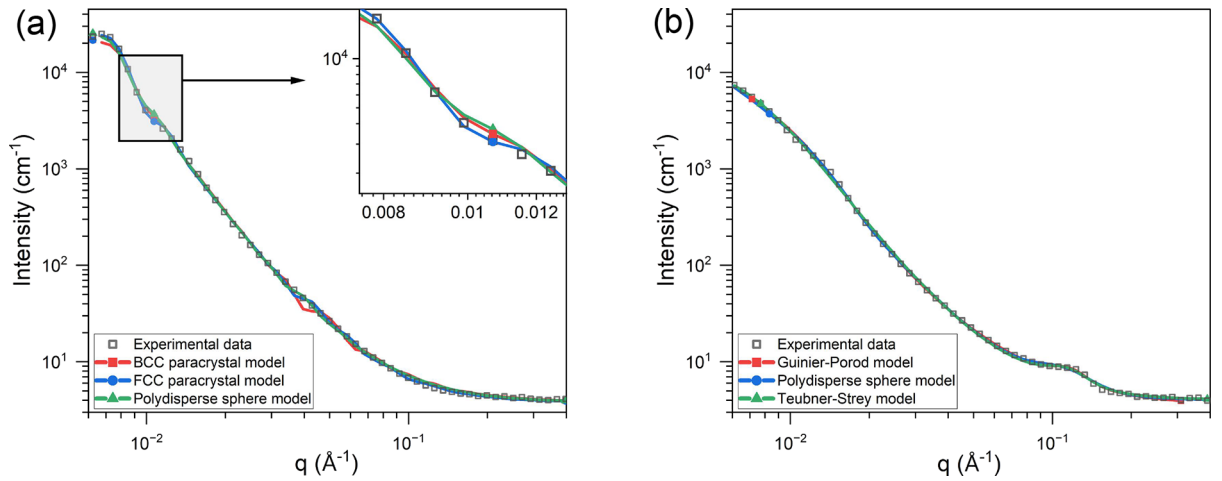


**Figure 7.** (a) Fitting quality comparison between a polydisperse spherical model, a BCC, and an FCC paracrystalline model for the high-$q$ part of the WB200-RT sample after 12 h of immersion. The models are summed to a Porod component to capture the change in the slope from $q$ >0.4 Å$^{-1}$. (b) Comparison of Guinier−Porod, Teubner−Strey, and polydisperse spherical models for the WB100-RT sample after 6 h of immersion. All models fit the sample reasonably well.

have been attributed to water presence between the colloids, hence highlighting the colloidal crystal packing.[33,34] In line with this, the low $q$ value peaks (peaks 1 in Figure 6b,c) are here ascribed to the scattering from water entering the crystalline-packed colloidal structure. The simplest model that describes the scattering from such systems is a polydisperse sphere model employing the Percus−Yevick (P−Y) approximation to calculate the structure factor.[37] Additionally, two paracrystal models (BCC and FCC paracrystalline models)[47] were also selected and implemented in SASView in order to identify the best fitting model. Both the spherical model with the P−Y structure factor and the FCC paracrystalline models yielded good fits to the main peak of the scattering function (Figure 7a), whereas the BCC paracrystalline model failed to provide a good fit. As such, the BCC model was not taken into any further consideration. This result aligns with previous studies reporting an FCC packing structure in waterborne acrylate films.[26,32,36]

A comparison of the resulting fitting parameters for the spherical and FCC paracrystalline models is presented in Table S2, while the fitting residuals for the various models are presented in Figure S4. Notably, the extracted particle radius is largely consistent across the two models, indicating that this parameter is model-agnostic and therefore unaffected by model biases. In contrast, the volume fraction exhibits a more significant variation, with the FCC paracrystalline model yielding values closer to those expected for perfect FCC particle packing, as recently observed in waterborne latexes.[34,48] Moreover, the FCC paracrystalline model better reproduces the shoulder observed in the scattering data, as highlighted in the inset of Figure 7a (blue line overlapping better with experimental black squares), as a result of its better ability to model different scattering peaks (Figure 7a) compared to that of the Percus−Yevick approach. The FCC paracrystalline model was therefore selected as the most suitable model.

The data in Figure 7 also present a subtle shoulder at high $q$ values, where the decay of the data does not follow the $q^{-4}$ decay expected for crystalline systems (Figure S5b for WB150-RT, Figure S5c for WB200-RT). To capture this shoulder, a Porod component was added to the fitting model, which represents scattering from diffuse, rough interfaces in the material.[31] The Porod model component clearly dominates the total model scattering fit at intermediate $q$ values ($0.04 \leq q \leq 0.1$). This is particularly evident for sample WB150-RT (Figure S5c), where the Porod component is dominant in almost all of the investigated $q$ ranges. WB150-RT samples also exhibit an upturn of the scattering intensity at very high $q$ values (feature (2) in Figure 6b). To capture this feature during fitting with physical models, it was necessary to introduce a broad peak function taken from Hammouda,[31] as low-$q$ upturn is not modeled by any of the models used to model the crystalline peak or the Porod model. Since no upturn in $q$ can be seen in WB200-RT samples, the broad peak model was not used to fit the data of these samples.

With the selection of the individual models, the composite fitting model for the WB200-RT data can then be written as

$$I = t \times [I_{\text{fcc-paracrystalline}} + I_{\text{Porod}}] + B \tag{3}$$

While the model for the WB150-RT samples adds a third component:

$$I = t \times [I_{\text{fcc-paracrystalline}} + I_{\text{Porod}} + I_{\text{peak}}] + B \tag{4}$$

$$I_{\text{Porod}}(q) = B/q^{n} \tag{5}$$

$$I_{\text{peak}}(q) = \left(\frac{C}{1 + (|q - q_0|\xi)^{a}}\right)^{b} \tag{6}$$

The main parameters in the $I_{\text{fcc-paracrystalline}}$ model[47] are the scale parameter A, the radius of the spheres $r_{\text{colloid}}$, the unit cell length $a$, and the paracrystalline distortion factor $d$, representing positional variations of the colloids from their ideal lattice positions. A Porod component and a broad peak model were added to capture features at higher $q$ values. The Porod contribution follows a simple power-law expression with a scale factor $B$ and exponent $n$. The peak function is an empirical form originally proposed by Hammouda[31] and subsequently applied in various polymer structure studies.[46] It is characterized by a scaling factor $C$, peak position $q_0$, and screening length $\xi$. Additionally, the function includes empirical shape parameters $a$ and $b$. In this study, these shape parameters were both set to 2 ($a = b = 2$) as this provided the best fit to the experimental data.


https://doi.org/10.1021/acs.langmuir.5c05519
Langmuir 2026, 42, 10205−10222

**Table 3. WB100-RT-Fitted Parameters**

| immersion time (hours) | WB100-RT | | | | | | | | |
|---|---|---|---|---|---|---|---|---|---|
| | $I_{Guinier-Porod}$ | | | | $I_{Porod}$ | | $I_{peak}$ | | |
| | $A$ ($mm^{-1}$) | $r_g$ (Å) | $s$ | $p$ | $B$ ($mm^{-1}$) | $n$ | $C$ ($mm^{-1}$) | $\xi$ (Å) | $Q_0$ ($Å^{-1}$) |
| 2 | 1.214 ± 0.003 | 118.5 ± 0.3 | 1 | 4 ± 0.01 | $0.0019 \pm 2 \times 10^{-5}$ | 1.95 ± 0.005 | 0.522 ± 0.003 | 25 ± 1 | $0.1340 \pm 7 \times 10^{-4}$ |
| 6 | 4.768 ± 0.007 | 132.2 ± 0.2 | 1 | 4 ± 0.01 | $0.0037 \pm 2 \times 10^{-5}$ | 1.98 ± 0.004 | 0.730 ± 0.003 | 31.6 ± 0.8 | $0.1145 \pm 3 \times 10^{-4}$ |
| 12 | 5.342 ± 0.007 | 137.2 ± 0.2 | 1 | 4 ± 0.01 | $0.003\,3 \pm 2 \times 10^{-5}$ | 2.00 ± 0.003 | 0.717 ± 0.003 | 45 ± 1 | $0.1112 \pm 2 \times 10^{-4}$ |
| 48 | 23.34 ± 0.03 | 154.3 ± 0.2 | 1 | 4 ± 0.01 | $0.0032 \pm 3 \times 10^{-5}$ | 2.19 ± 0.005 | 0.864 ± 0.003 | 39.1 ± 0.9 | $0.0965 \pm 2 \times 10^{-4}$ |

Contrary to the polymers made with medium and high colloidal particle sizes, the WB100-RT samples (Figure 6a) do not show a clear low-$q$ peak. As a result, fitting with the paracrystalline models was not possible as these models naturally result in a clear peak in the scattering intensity. Given the lack of a clear physical origin behind the scattering intensity, the Guinier−Porod model was employed instead. Other fits with more physics informed models, such as the Teubner−Strey and a polydisperse dilute spherical model (shown in Figure 7b), led to similar or worse fitting qualities while resulting in comparable parameters such as the characteristic dimension (Table S3). Since the characteristic dimension of this feature is too small to be related to the colloidal size and to be easily attributed to a known physical feature, the shape-agnostic Guinier−Porod model was finally selected, hence avoiding the imposition of an arbitrary shape to the feature.

Besides the Guinier−Porod model, an additional Porod component was added to capture the slope change at intermediate $q$ values, as also observed in WB200-RT and WB150-RT films. The impact of this second component can be seen in Figure S5a. Similarly to WB150-RT samples, a clear upturn in the high-$q$ scattering intensity was observed (peak "2" in Figure 6a).

As a result of the model selection process, the composite model selected for the WB100-RT samples can be written as (Figure 6a)

$$I = t \times [I_{Guinier-Porod} + I_{Porod} + I_{peak}] + B \tag{7}$$

$$I_{Guinier-Porod}(q) = \begin{cases} \dfrac{A}{q^s}\exp\left[\dfrac{-q^2R_g^2}{3-s}\right], & q < Q_1 \\ D/q^p, & q \geq Q_1 \end{cases} \tag{8}$$

where $I_{Porod}$ and $I_{peak}$ follow eqs 5 and 6, respectively. The Guinier−Porod model was proposed by Hammouda[49] and accounts for scattering from objects characterized by a dimensionality $s$, a radius of gyration $R_g$, and a Porod exponent $p$. The scale parameter $A$ serves as the scaling factor and is influenced by the scattering length contrast between the features and the surrounding matrix as well as the volume fraction of the features. $D$ and $Q_1$ are model parameters chosen to ensure the continuity of the model and its derivatives.[49]

With the composite models selected for each film type, the fitting of the data obtained at all immersion times in deuterated water was performed. Tables 1−3 show the characteristic fitting parameters and their variation with the exposure time (see Table 4).

## Film Microstructure Reconstruction Based on SANS Fitting Models as a Function of Immersion Time

The selected fitting models allow us to provide insight into the film microstructure and its dependency on the colloid particle size.

Figure 8 plots the fitting parameters from Table 5 obtained for the big colloid size of 200 nm (WB200-RT) as a function of immersion time. The presence of the peak "1" in Figure 6c, captured mainly through the FCC paracrystalline model, represents water entering through the hydrophilic paths surrounding the colloid cores, highlighting the colloidal crystalline packing.[33,34] We refer to the volume of the material between the colloids as the colloid−colloid interphase, as it represents a phase where the polymer chains from the colloidal cores have interdiffused, binding the polymer together and yielding an (inter)phase with different and chemical properties from the bulk of the particles.[27,50−52] As the immersion time increases, water is seen first entering and filling the colloid−colloid interphase, reducing the radius of the dry region of colloidal cores and yielding the detected decrease in the particle size (Figure 8a). The water also swells the interphase, which is observed as an increase in the crystal lattice parameter (distance between the colloid cores) in Figure 8a. Finally, an increase in the scale value of the paracrystalline model is observed (parameter A, Table 5, Figure S6c). This can be explained by both an increase in the scattering length contrast, due to the presence of more and more deuterium in the interphase, and an increase in the relative volume fraction of the crystalline structure highlighted by the entering deuterium. The latter effect should be particularly prominent at lower absorption times, as we expect a gradient in the concentration of deuterium across the thickness of the films and a step process of diffusion along the channel (shorter times), followed by swelling (at longer times).

The additional Porod term in the fitted model, dominant at intermediate $q$ values ($0.04 \leq q \leq 0.1$), captures the finer details of the colloid−colloid interphase. A deviation from the traditional Porod exponent of $n \sim 4$ indicates the presence of rough structures of varied size. An increase in the exponent $n$ (Figure 8b) reflects the filling and swelling of the colloid−colloid interphase, which evolves from a 2-dimensional structure (thin membrane between the colloids) to a rougher, 3-dimensional structure (thick interphase between the colloids). The roughness in this context indicates a locally heterogeneous distribution of deuterium at the interphase, probably related to the local position of the surfactant and polymer chains. The increase in the scale parameter (Figure 8b) can be caused by an increase in the scattering length density or a change in the surface area of the deuterated volume.

The resulting structure of WB200-RT films responsible for water transport is visualized in Figure 9 to highlight the presence of colloid−colloid hydrophilic interphases for water transport.



https://doi.org/10.1021/acs.langmuir.5c05519
Langmuir 2026, 42, 10205−10222

Table 4. WB150-RT-Fitted Parameters

| | WB150-RT | | | | | | | | | | | |
|---|---|---|---|---|---|---|---|---|---|---|---|---|
| | $I_{fcc\text{-}paracrystalline}$ | | | | $I_{Porod}$ | | | $I_{peak}$ | | | | |
| immersion time (h) | $A$ (mm$^{-1}$) | $a$ (Å) | $d$ | $R$ (Å) | $B$ (mm$^{-1}$) | $n$ | | $C$ (mm$^{-1}$) | $\xi$ (Å) | $Q_0$ (Å$^{-1}$) | | |
| 2 | 0.0305 ± 2 × 10$^{-4}$ | 1728 ± 3 | 0.0428 ± 8 × 10$^{-4}$ | 603.9 ± 0.6 | 9.16 × 10$^{-5}$ ± 5 × 10$^{-7}$ | 3.000 ± 3 × 10$^{-3}$ | | 0.549 ± 2 × 10$^{-3}$ | 14.9 ± 0.5 | 0.0989 ± 9 × 10$^{-4}$ | | |
| 6 | 0.0342 ± 2 × 10$^{-4}$ | 1692 ± 2 | 0.047 ± 1 × 10$^{-3}$ | 598.6 ± 0.7 | 9.93 × 10$^{-5}$ ± 5 × 10$^{-7}$ | 3.105 ± 2 × 10$^{-3}$ | | 0.517 ± 2 × 10$^{-3}$ | 18.7 ± 0.5 | 0.0920 ± 7 × 10$^{-4}$ | | |
| 12 | 0.0838 ± 2 × 10$^{-4}$ | 1679 ± 1 | 0.0520 ± 4 × 10$^{-4}$ | 636.8 ± 0.2 | 9.95 × 10$^{-5}$ ± 4 × 10$^{-7}$ | 3.200 ± 2 × 10$^{-3}$ | | 0.557 ± 3 × 10$^{-3}$ | 24.3 ± 0.9 | 0.0820 ± 7 × 10$^{-4}$ | | |
| 48 | 0.0413 ± 9 × 10$^{-4}$ | 1690 ± 1 | 0.031 ± 1 × 10$^{-3}$ | 632.7 ± 0.5 | 6.93 × 10$^{-5}$ ± 3 × 10$^{-7}$ | 3.505 ± 2 × 10$^{-3}$ | | 0.799 ± 2 × 10$^{-3}$ | 15.4 ± 0.3 | 0.0612 ± 9 × 10$^{-4}$ | | |

The time-dependent interphase swelling and associated decrease in water-poor polymer phase size (i.e., colloid cores) highlights a preferential diffusion of water through the interphases into the polymer rather than homogeneously diffusing through the whole polymer film from the exposed surface.

Figure 10 plots the SANS fitting parameters for the small colloidal size WB100-RT. The most prominent feature is the peak labeled as "2" in Figure 6a. In agreement with previous works reporting the presence of similar peaks in comparable systems (e.g., sulfonated-surfactant aggregation in waterborne acrylic polymers[53] and sulfate-surfactant aggregation[54−56]), we relate the presence of this peak to surfactant aggregation responsible for the creation of well-defined pockets of deuterated water. The peak increases both in height (Figure 10c) and width (Figure 10d), while shifting to lower Q values (Figure 10e) as water enters the material. The increase in height indicates an increase in the deuteration level (concentration of $D_2O$) of the pockets, while the change in the width and position is related to the growing and merging of the water pockets with increasing immersion times.

The scattering intensity also exhibits an inflection at low $q$ values (point "1" in Figure 6a), captured by the Guinier−Porod model. The slope at low-$q$ values determines the $s$ parameter of the Guinier−Porod model, which was found to best fit the model when $s = 1$ (Table 3), indicating a one-dimensional shape, like a needle or elongated rod. The one-dimensional nature of these rods suggests the presence of elongated channel-like features through which the deuterated water permeates the material. The radius of gyration $R_g$ of the Guinier−Porod model increases with the water absorption time (Figure 10a), suggesting a lateral increase in the size of these channels (i.e., swelling of the channels due to deuterated water absorption). The Guinier−Porod exponent $p = 4$ (Table 3) denotes Porod behavior, indicating a relatively smooth transition between deuterated and nondeuterated areas of the material, pointing at a relatively sharp transition region between the water-rich channel-like features and the surrounding water-poor matter (polymer). This smoothness indicates a relatively large difference in hydrophilicity between the channels and surrounding polymer matrix, owing to lower entanglement density as well as the presence of surfactant aggregates. The increase in Guinier−Porod scale parameter A (Table 3, Figure S6a) indicates either an increase in the scattering length contrast or an increase in the volume fraction of channels, possibly driven by further penetration of the deuterium across the thickness of the films.

The slight upturn of the scattering intensity in WB100-RT samples observed at low-$q$ (Figure 6d, zoomed-in view of Figure 6a) suggests that a small portion of the water enters through the colloid−colloid interphases dominating the water transport in the WB200-RT samples. This is supported by the presence of a shoulder modeled by a Porod model with exponent $n \sim 2$ (Table 3) similar to the WB200-RT samples (Figure 10b). The exponent $n$ does not reach the same values as the exponent calculated for larger particle sized samples (Table 5), indicating that the interphase appears more stable and does not grow into a rough domain in the material. The saturation of scale parameter B (Figure 10b) further indicates a stable deuterium/hydrogen ratio within the interphase, which is compatible with a strong colloid−colloid interphase that does not swell to accommodate increasing amounts of $D_2O$.

As a result of the interpretation of the characteristic parameters resulting from the fitting model used WB100-RT



https://doi.org/10.1021/acs.langmuir.5c05519
Langmuir 2026, 42, 10205−10222

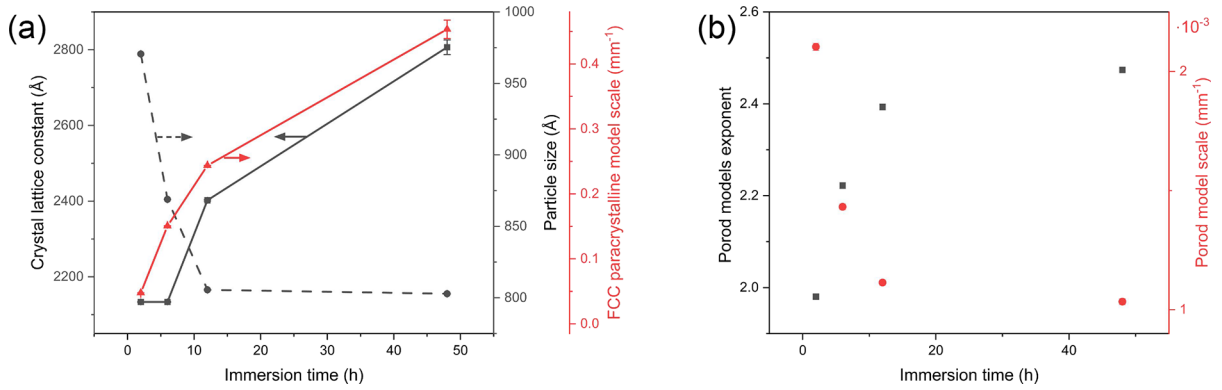


**Figure 8.** Variation of the fitting parameters of the WB200-RT sample as a function of the immersion time. (a) Particle size R, crystal lattice parameter a and paracrystalline model scale A and (b) scale and exponent of the Porod model n.

**Table 5. WB200-RT-Fitted Parameters**[a]

| immersion time (hours) | WB200-RT | | | | | |
|---|---|---|---|---|---|---|
| | $I_{\text{fcc-paracrystalline}}$ | | | | $I_{\text{Porod}}$ | |
| | $A$ (mm$^{-1}$) | $a$ (Å) | $d$ | $R$ (Å) | $B$ (mm$^{-1}$) | $n$ |
| 2 | $0.04769 \pm 6 \times 10^{-5}$ | $2134 \pm 1$ | $0.0655 \pm 5 \times 10^{-4}$ | $970.6 \pm 0.2$ | $0.00210 \pm 2 \times 10^{-5}$ | $1.980 \pm 0.005$ |
| 6 | $0.1506 \pm 3 \times 10^{-4}$ | $2134 \pm 1$ | $0.0378 \pm 2 \times 10^{-4}$ | $868.9 \pm 0.1$ | $0.00143 \pm 1 \times 10^{-5}$ | $2.082 \pm 0.004$ |
| 12 | $0.243 \pm 3 \times 10^{-4}$ | $2402 \pm 2$ | $0.0800 \pm 7 \times 10^{-4}$ | $805.6 \pm 0.1$ | $0.00111 \pm 1 \times 10^{-5}$ | $2.393 \pm 0.007$ |
| 48 | $0.435 \pm 0.002$ | $2452 \pm 5$ | $0.139 \pm 0.001$ | $802.83 \pm 0.08$ | $0.00103 \pm 1 \times 10^{-5}$ | $2.199 \pm 0.003$ |

[a]The model did not use a peak function because there is no high-$q$ peak in these samples (Figure 6a).

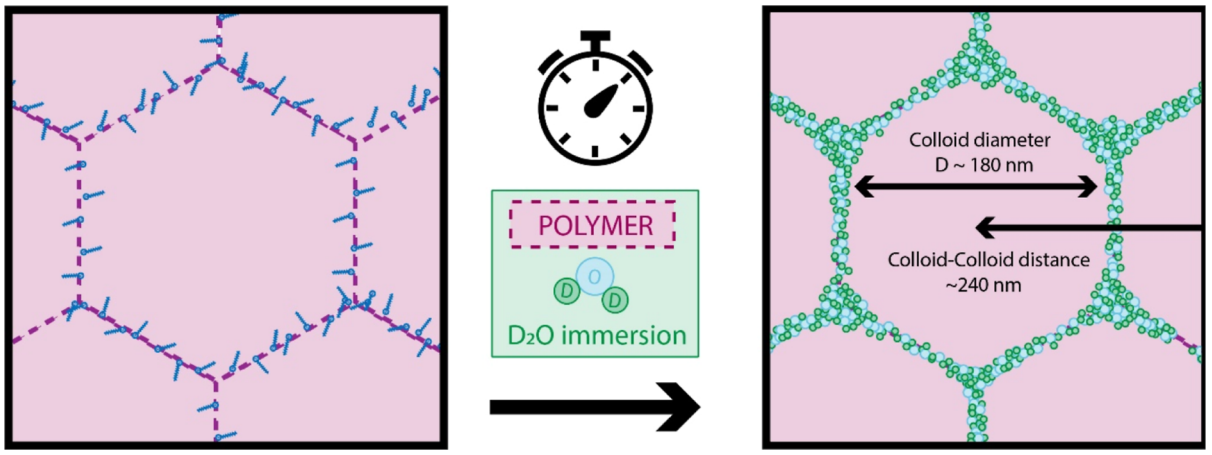


**Figure 9.** Structure of the WB200-RT samples. The deuterated water penetrates through the colloid−colloid interphase, highlighting the crystal structure of the samples. The interphase is swollen with water absorption.

sample, we propose the structure shown in Figure 11 with the following two governing features for water transport: (1) segregated hydrophilic channels of ∼15 nm width, likely created by surfactant aggregation facilitating rapid water transport, and a smaller contribution to the water uptake of (2) remnant colloid−colloid hydrophilic interphases.

Figure 12 shows the characteristic fitting parameters of the film WB150-RT. In line with the previous discussion and proposed microstructure models for 100 and 200 nm films, the data suggest the presence of water uptake at colloid−colloid interphases (peak "1" in Figure 6b), corroborated by the good agreement between the colloid radius calculated through the FCC paracrystalline model (∼65 nm, Figure 12a) and the colloidal radius measured through DLS (75 nm, Table 1). Moreover, the appearance of a shoulder peak "2" in Figure 6b suggests the existence of features in the range of 4 nm compatible with the presence of water clusters attributed to local surfactant aggregation (Figure 12c−e), which follow a similar evolution to film WB100-RT (Figure 10c−e).

The colloid−colloid interphases do not appear to be as defined as those in the WB200-RT samples; this is highlighted by the absence of a shoulder next to the peaks (Figure 6b). The lack of a significant increase in the crystal lattice parameter or reduction in colloidal particle size (Figure 12a) indicates that water does not swell the colloid−colloid interphase, nor does it significantly penetrate within the colloidal cores as observed for the WB200-RT films. The lower crystal peak scale A (Figure S6b) and lack of increase with time compared to samples of WB200-RT support this hypothesis.

Instead, the water appears to form a complex structure within the interphase, forming a peak (peak "2" in Figure 6b) that resembles the peak found in WB100-RT samples. The


https://doi.org/10.1021/acs.langmuir.5c05519
Langmuir 2026, 42, 10205−10222

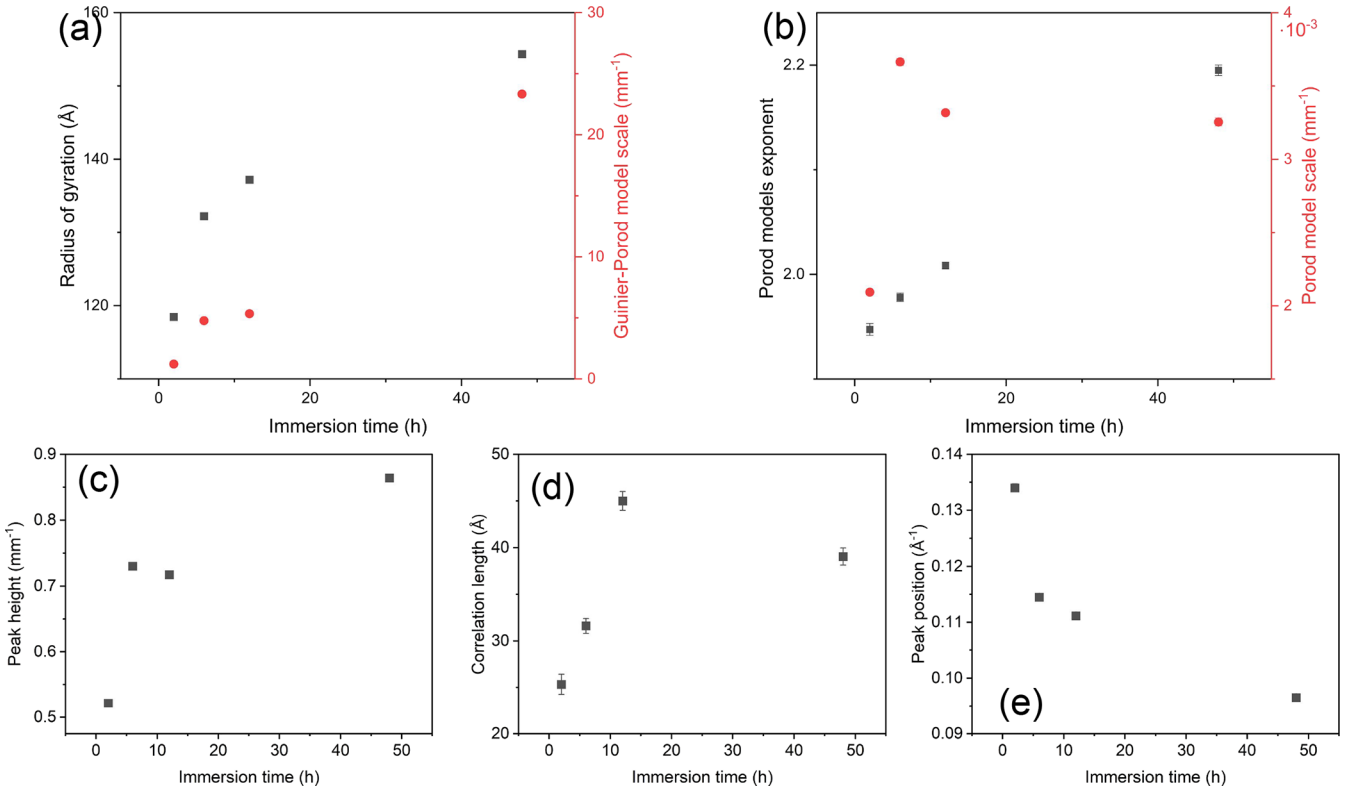


**Figure 10.** Variation of the fitting parameters of the WB100-RT sample as a function of the immersion time. (a) Scale of the Guinier−Porod model A and$R_g$ of the Guinier−Porod model; (b) scale of the Porod model B and exponent n; (c) peak height C, (d) correlation length $\xi$, and (e) peak position $q_0$ of the broad peak model.

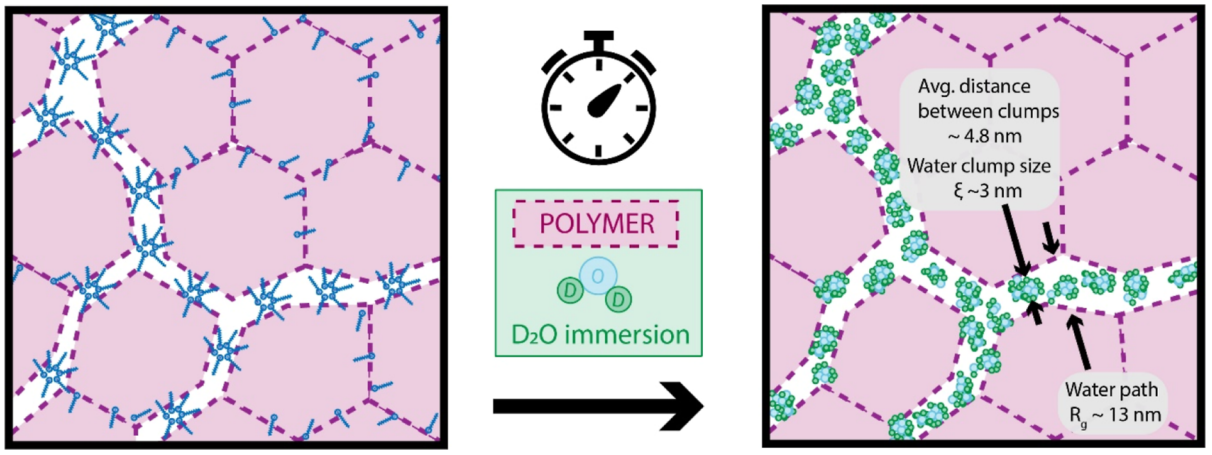


**Figure 11.** Structure of the WB100-RT samples. The channels correspond to the lower $q$ feature, while the structure of the deuterated water within the channels corresponds to the higher $q$ peak. The channels are swollen with water absorption.

correlation length of the high-$q$ peak (Figure 12d), akin to a characteristic size for the feature, is slightly smaller than for the WB100-RT samples (Figure 10e), indicating the water pockets are smaller in the WB150-RT samples. Moreover, the peak has a lower prominence in WB150-RT samples than in WB100-RT samples (Figure 6b,a), indicating a lower scattering contrast with the surrounding medium. All of this is compatible with the presence of water pockets existing within a colloid−colloid interphase, which also acts as a hydrophilic pathway similar to the WB200-RT samples. The Porod component, with an exponent going from $n$ ~3 to $n$ ~4 (Figure 12b), reveals the presence of an initially rough distribution of water within the interphase. This is compatible with the presence of surfactant aggregates at the interphase leading to a highly locally heterogeneous distribution of deuterium at the interphase. The transition toward $n$ ~4 indicates that the deuterium saturates the interphase, yielding a more locally smooth and homogeneous deuterium distribution within the interphase. This is supported by the decrease in the scale of the Porod model (Figure 12b), suggesting that the shoulder tends to disappear within the $q^{-4}$ decay of the paracrystalline model. This is also reflected in the disappearance of peak "2" at higher immersion times. As a result, a model structure showing hydrophilic colloid−colloid interphases with local water pockets representative of the WB150-RT films is shown in Figure 13.


https://doi.org/10.1021/acs.langmuir.5c05519
Langmuir 2026, 42, 10205−10222

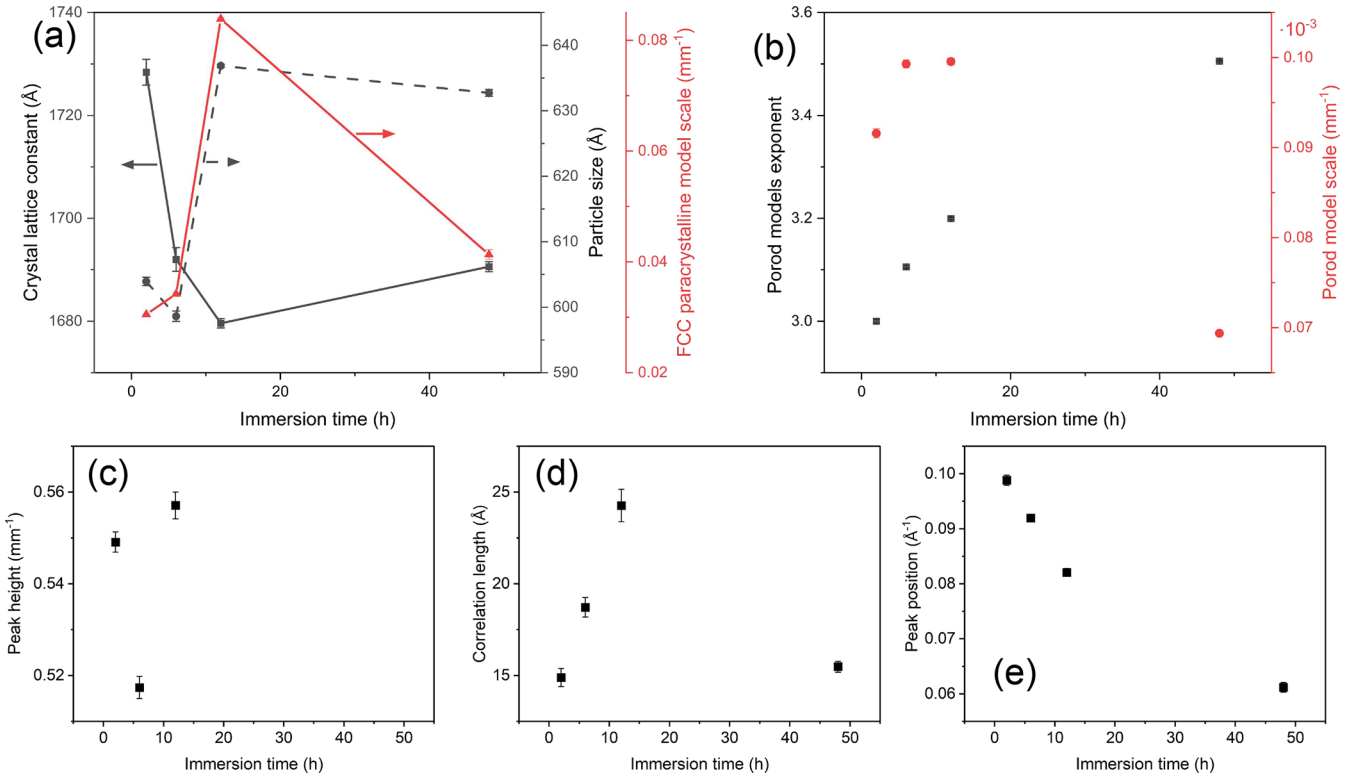


**Figure 12.** Variation of the fitting parameters of the WB150-RT sample as a function of the immersion time. (a) Scale A, particle size and crystal lattice parameter of the FCC paracrystalline model; (b) scale B and exponent n of the Porod model; (c) peak height C, (d) correlation length $\xi$, and (e) peak position $q_0$ of the broad peak model.

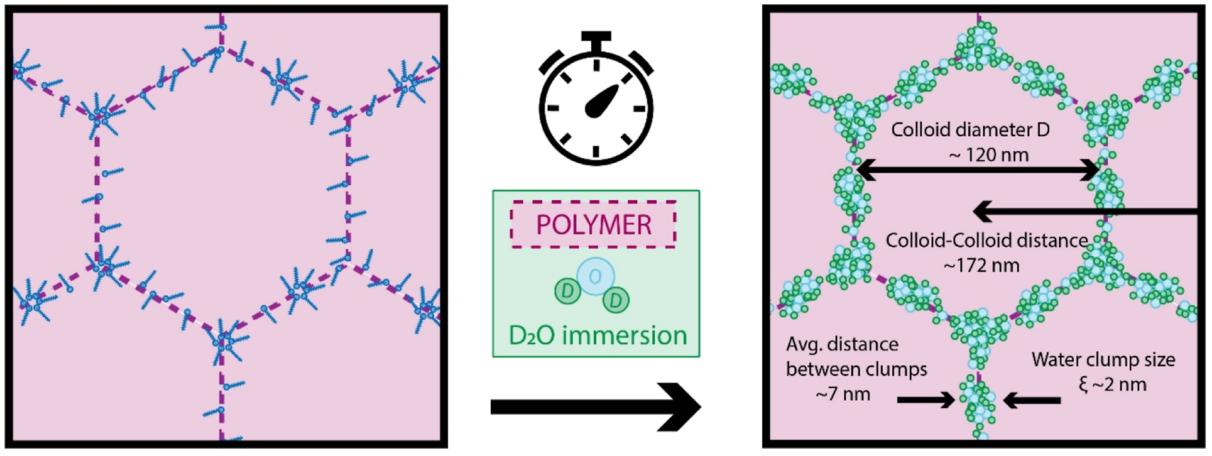


**Figure 13.** Structure of the WB150-RT samples. The deuterated water highlights the crystal structure by aggregating at surfactant sites without fully penetrating the colloid−colloid interphase. With time, the deuterated water penetrates through more of the colloid−colloid interphase.

## Eliminating Colloid−Colloid Interphases through Annealing

To further confirm the models derived from the SANS analysis, the films were annealed at 50 and 80 °C for 24 h to increase chain interdiffusion in the rubbery state and decrease the presence of colloid−colloid interphases and surfactant clusters. After annealing, the samples were left to cool down slowly and exposed to water to perform SANS. All the films were fitted with the same models as the respective nonannealed films, removing components when necessary.

The results for films WB200-50C and WB200-80C can be found in Figure 14 and Table S4. The scattering profile of the sample annealed at 50 °C is highly comparable to that of the WB200-RT samples, including similar well-defined peaks (Figure 14a, Figure 6c), and therefore a comparable structure for water transport. Nevertheless, the particle size (i.e., colloid) obtained with the FCC paracrystalline model is slightly higher (~90 nm) than that of the nonannealed polymers (~80 nm) (Figures 15a, 8b) and the crystal lattice parameter (colloid distance) does not increase with immersion time (Figure 15a). Moreover, scale parameter A (Figure S7) is lower for each increase in annealing temperature, indicating that a lower amount of deuterium is present within the film. All this suggests that the annealing process resulted in smaller and less-prone to swelling colloid−colloid interphases, likely due to a higher degree of interdiffusion, entanglement, and homogenization.


https://doi.org/10.1021/acs.langmuir.5c05519
Langmuir 2026, 42, 10205−10222

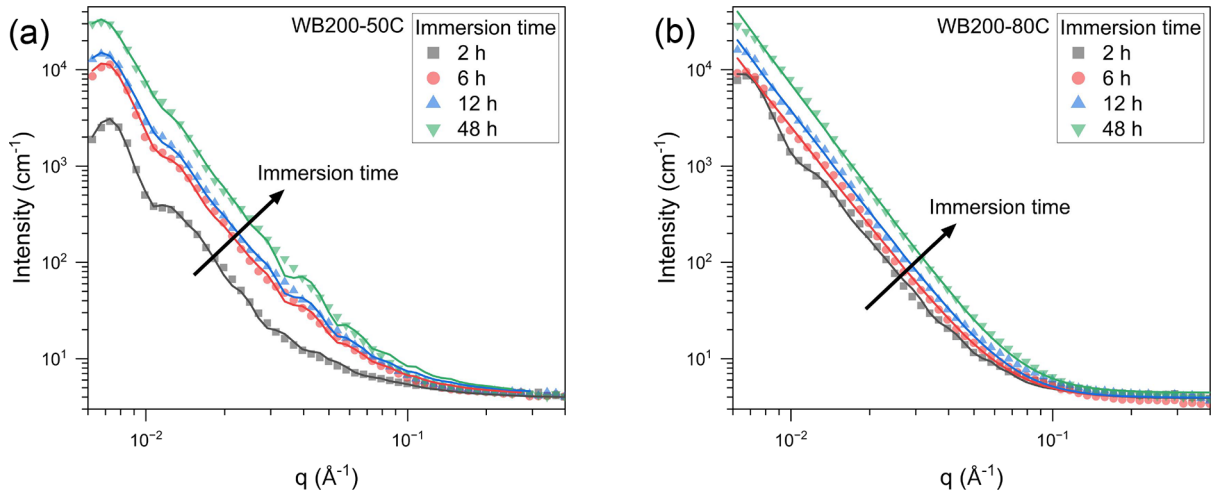


**Figure 14.** Results for the (a) WB200-50C1D and (b) WB200-80C1D samples. Points: experimental data, Solid lines: fits. The peak characterizing the colloidal crystal structure becomes less prominent with an increase in the annealing temperature, indicating that the colloid−colloid interphase is being homogenized by the diffusion of the polymer chains.

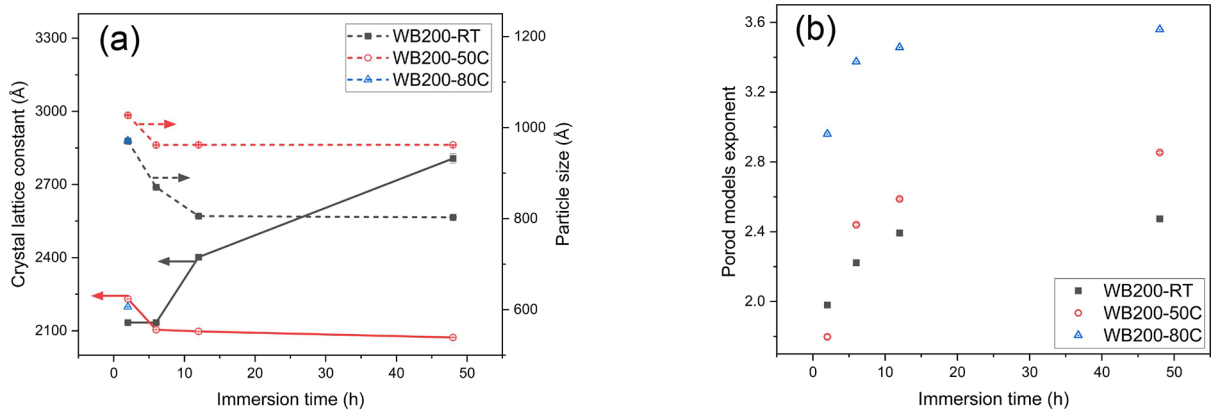


**Figure 15.** Comparison of the fitting parameters for as-prepared samples (red circles) and 80 °C annealed samples (blue triangles) as a function of water immersion time for WB200 samples. (a) Crystal lattice parameters, and (b) Porod model exponent.

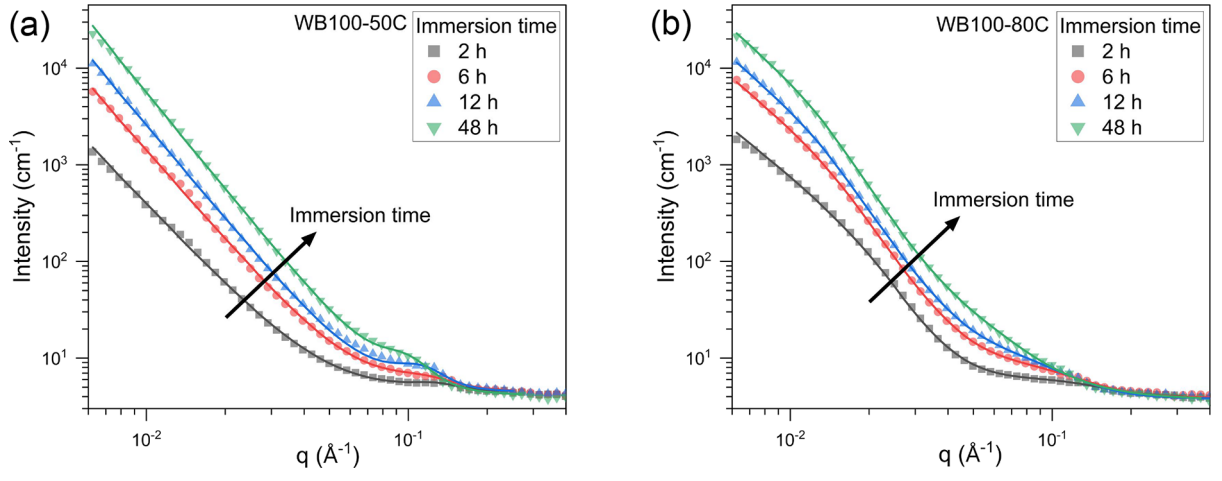


**Figure 16.** Results for the (a) WB100-50C1D and (b) WB100-80C1D samples. Points: experimental data, Solid lines: fits. The peak characterizing the colloidal crystal structure becomes less prominent with an increase in the annealing temperature, indicating that the interphase is being homogenized by the diffusion of the polymer chains.

The increased Porod component exponent (Figure 15b) suggests that more water started entering within the particle cores, increasing the slope of the scattering intensity and the deviation from Porod behavior.

Unlike for the samples annealed at RT and 50 °C, when the samples were annealed at 80 °C (sample WB200-80C), the characteristic dimensional peaks are barely visible at very short immersion times (Figure 14). After 12 h of immersion, the



https://doi.org/10.1021/acs.langmuir.5c05519
Langmuir 2026, 42, 10205−10222

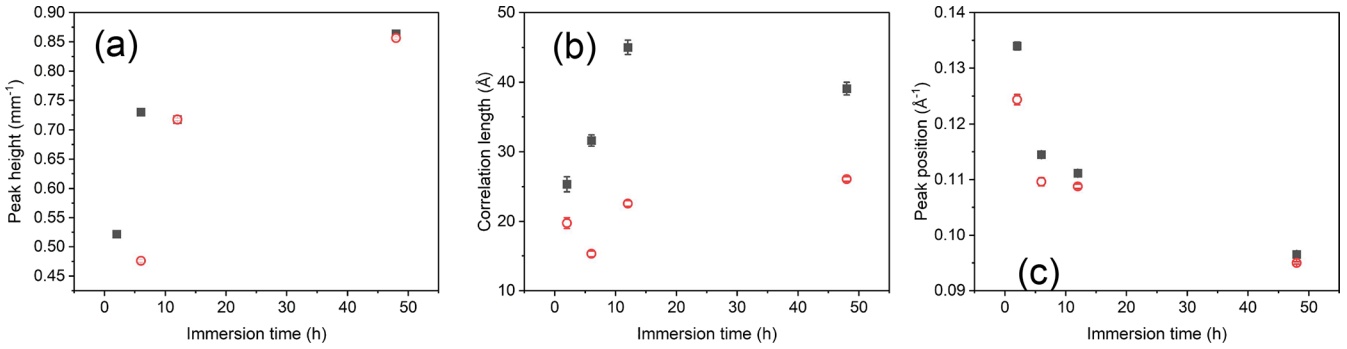


**Figure 17.** Comparison of the fitting parameters for as-casted (black circles) and 50 °C annealed samples (red squares) as a function of water immersion time for WB100 samples. (a) Peak height C, (b) correlation length $\xi$, and (c) peak position $q_0$ of the broad peak model.

deuterated water penetrated the polymer largely homogeneously up to the point of making the peaks indistinguishable from the baseline Porod law scattering typical of a polymer. All in all, the results suggest that annealing the films created from 200 nm colloids at 80 °C for 1 day results in a high level of homogenization yet maintaining the presence of colloid−colloid interphases up to a certain level.

The annealing protocol created more pronounced differences when it was applied to the WB100 dispersion samples. A 50 °C annealing (Figure 16a) induced the disappearance of the low-$q$ feature in the WB100-RT related to the presence of water channels (Figure 6a). Instead, the water appears to be concentrated in the water clusters created by surfactant aggregates, which are similar in height (Figure 17a) and position (Figure 17c) to those found in the nonannealed samples, with small differences (∼1 nm) in correlation length (Figure 17b) attributable to suboptimal fit of the peak shape. The undulations seen in the WB100-RT sample (Figures 16a, 6d) are also present in the scattering spectra of the annealed samples, hence confirming that 50 °C annealing for 1 day is insufficient to completely remove the colloid−colloid interphases.

At 80 °C, the scattering profile of the films made from 100 nm colloids changed significantly. As shown in Figure 16b, the fitting procedure revealed the presence of a structure with a characteristic length increasing from ∼4 to ∼6 nm with immersion time (Table S5). Even if the colloid−colloid interface characteristic peak is not present, the "s" parameter of the Guinier−Porod model controlling the low-$q$ slope was found to be $s$ ∼2, which indicates a two-dimensional structure compatible with the presence of remnants of the colloid−colloid interphases.

These results highlight how, even after a relatively aggressive annealing, the colloid−colloid interphases still play an important role in water transport, shaping especially the water pathways in the early stages of water absorption. This is attributed to the limited mobility of the surfactant within the polymer matrix, resulting in the permanent entrapment of hydrophilic surfactants at the colloid−colloid interphases, thereby creating permanent pathways for preferred water transport.

## Relation between Water Uptake and Film Microstructure

Figure 18 summarizes the key findings of the work and relates water uptake, DVS data, and SANS-derived film microstructure as a function of the colloid particle size.

A clear correlation can be seen between the SANS structure and the different moisture sorption behaviors observed through DVS and gravimetric water absorption experiments. A careful analysis of the SANS data showed how the main pathway for water absorption in films formed with small colloids (∼100 nm particle size) is relatively wide (∼15 nm in diameter, Table 3), highly hydrophilic channels likely created by surfactant segregation (Figure 10). While always present, these channels tend to homogenize (become more compact and smaller) with annealing (e.g., 50 °C, 1 day). We hypothesize these channels originate as defects in the colloidal crystal packing structure during drying, where the surfactant desorbed from the colloidal cores accumulates and gets rapidly trapped by the film formation. Surfactant-rich defects are expected to hinder chain interdiffusion in these areas, hence leading to local higher free volume and lower density. As observed with SANS, these channels offer fast pathways for water absorption, explaining the trends observed in the sorption isotherm (Figure 2a): the increase in the monolayer water mass $m_m$ (Figure 4a), the decrease in the energy associated with adsorption ($C_{BET}$) (Figure 4b), and the increase in the tendency of forming water clusters (Figure 4d). As the channels and surfactant aggregates are saturated with sorbed moisture, further moisture sorption is slowed (Figure 3a). At the 80 °C annealing temperature, there is sufficient energy available for chain and surfactant movement to change the structure of the polymers, resulting in a broad change in the slope of the scattering intensity (Figure 16b), possibly related to some remnants of the colloid−colloid interphase between the particles. Unlike for other films, the colloid−colloid interphase in the annealed or not annealed WB100-RT samples remains barely visible (Figure 6a), therefore suggesting that the particles are relatively well coalesced and interdiffusion is almost completed at this colloidal size. The presence of the hydrophilic channels is likely responsible for the rather high gravimetric water absorption (Figure 1a).

For the coatings created with the 200 nm colloids (WB200-RT, Figure 9), the SANS data show clear peaks characteristic of a crystal FCC structure (Figure 6c) in the absence of other water transporting features, hence implying that water enters through the colloid−colloid interphases. The sorption isotherm equally reflects this effect, as the larger particle-sized samples show decreased water affinity and decreased water clustering (Figure 2c). The fitting of the SANS peak and the nearby shoulder (Figure 6c) showed a rapid saturation of water at the colloid−colloid interphase, after which the majority of the water does not penetrate the particle cores but instead starts swelling the colloid−colloid interphase region (increase in the lattice parameter and plateauing of the particle size in Figure 8a). This suggests that the colloid−colloid interphases are relatively more hydrophilic than the bulk core and the interphases in films made from smaller colloids (as these remain non swollen). Despite having a more water-sensitive colloid−colloid inter-


https://doi.org/10.1021/acs.langmuir.5c05519
Langmuir 2026, 42, 10205−10222

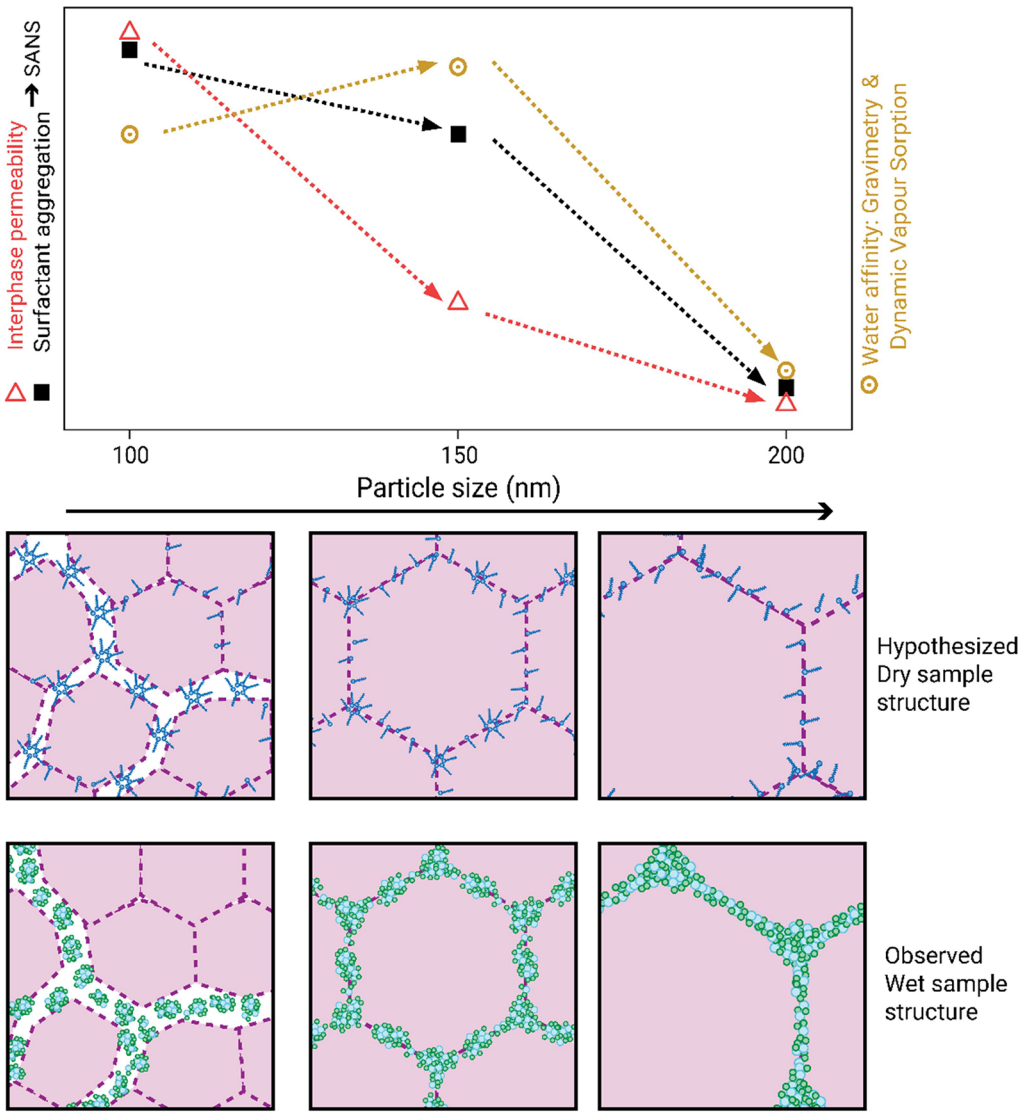


**Figure 18.** Figure shows the different film structures as a function of the colloid particle size. A hypothesized dry structure is presented as a result of the analysis. Macroscopic film water uptake properties show a direct relation with the availability of surfactant sites for water absorption, with intermediate-size colloids showing the highest availability of surfactant through surfactant aggregation and a weaker colloid−colloid interphase than smaller colloidal sizes. Large colloids, despite showing the weakest colloid−colloid interphase (which creates preferential water transport pathways), show lower macroscopic water absorption due to the lack of surfactant aggregation. For small colloids: $R_{g,\ paths}$ ~13 nm, $D_{surf.aggregates}$ ~3 nm, $d_{aggregates}$ ~5 nm; for medium colloids: $d_{colloids}$ ~172 nm, $D_{colloids}$ ~120 nm, $D_{surf.aggregates}$ ~2 nm, $d_{aggregates}$ ~7 nm, for big colloids: $d_{colloids}$ ~240 nm, $D_{colloids}$ ~18 0 nm.

phase than films formed from smaller particle sizes, the surfactant is well dispersed as evidenced by the lack of a high-$q$ peak. This is related to a lower water affinity (Figure 2c) and lower water−water clustering (Figure 4d) as measured by DVS and the lowest water uptake of all of the samples (Figure 1). The lower affinity of the colloid−colloid interface compared to the highly hydrophilic paths in WB100-RT samples leads to the lower latex−water diffusion coefficient and possibly its lower dependence on relative humidity (Figure 3) for these samples. Annealing of these films at 50 °C led to a colloid−colloid interphase apparent strengthening (Figure 14a) as observed by an increased dry colloid core radius (Figure 15a) and water diffusing into the particle cores instead of swelling the interphase (Figure 15a). The colloid−colloid interphase strengthening effect is attributed to a higher chain interdiffusion at the interphases, while the hydrophilic surfactant remains trapped at the colloid−colloid interphase. An 80 °C annealing temperature further strengthened the interphase and homogenized the surfactant. As a consequence, water enters the particle cores and is homogeneously transported through the polymer after 12 h of immersion time (Figure 14b).

Intermediate particle sizes (WB150, Figure 13) appear to create an intermediate structure with stronger colloid−colloid interphases that do not swell with water (Figure 12a), unlike WB200-RT samples but similar to the 100 nm ones (Figure 8b). The samples also show a high-$q$ peak characteristic of surfactant aggregates not observed in the 200 nm but observed in the 100 nm (Figure 6b), albeit without the large-scale heterogeneities seen in the WB100-RT samples (Figure 6a). The combination of both surfactant aggregates as well as a clearly hydrophilic interphase seems to yield the highest water affinity (Figure 2b) and an increased water absorption (Figure 1b) as graphically represented in Figure 18.

An increase in the mobility of the surfactant during the drying stage can help explain the mechanism controlling surfactant aggregation. The Routh−Russell map[1,57,58] showcases how an


https://doi.org/10.1021/acs.langmuir.5c05519
Langmuir 2026, 42, 10205−10222

increase in particle size is expected to reduce the colloid mobility and deformability, shifting the predominant drying mechanism from wet to moist/dry sintering. Computational models[12] demonstrated that a higher amount of water retained in the coating during the particle deformation stage leads to a higher surfactant mobility. We can therefore hypothesize that an increase in particle size leads to a decrease in the surfactant mobility, trapping the surfactant on the colloidal surfaces and consequently in the colloid−colloid interphases in the dry film. On the other hand, smaller colloidal sizes increase the surfactant mobility, allowing the desorbed surfactant to aggregate. These aggregates can then hinder chain interdiffusion and create the fast water transport pathways observed in the WB100-RT samples.

## CONCLUSIONS

In this paper, water transport pathways in waterborne colloidal films have been studied by using SANS, DVS, and gravimetry. A careful fitting protocol of the SANS data allowed observing the evolution of the distribution of water within the films with time, highlighting a complex structure of water transport pathways varying as a function of the colloidal particle size. In turn, the different water pathways explained well the macroscopic trends in water absorption and water affinity observed through gravimetry and DVS.

The colloid size was the main parameter used to affect the water transport pathways. It was found that films from larger colloids promote water transport through the colloid−colloid interphase. Decreasing the colloid size led to a reduction in the water permeability of the colloid−colloid interphase, as well as an increase in the aggregation of the surfactant. The surfactant aggregates were found to be located at the colloid−colloid interphase for intermediate colloid sizes and in wider channels in films made with yet smaller colloid sizes. Surfactant aggregation yields an increase in hydrophilic sites available for water uptake, increasing the macroscopic water affinity and uptake, as seen by DVS and gravimetry. Intermediate colloidal sizes led to the combination of a relatively permeable colloid−colloid interphase and relatively mild surfactant aggregation, resulting in the highest water uptake and permeability of the films analyzed. While the structural features identified in this work that are responsible for water transport may be universal, it should be noted that different film formation processes for the same particle sizes may lead to different features in the different films. Moreover, although the SANS data presented here provide a robust bulk average, complementary studies are required to resolve the structural profile across the film thickness.

Even though the particle size is not the only factor affecting colloidal packing and the film structure, shedding light on the different kinds of heterogeneities present in waterborne coatings and their influence on the water transport offers unique information to understand anticorrosive behavior of waterborne films and opens the possibility to further improve waterborne coatings by tailoring the water transport pathways to specific applications, thereby increasing the applicability of waterborne binders in anticorrosion coatings.

## ASSOCIATED CONTENT

### Supporting Information

The Supporting Information is available free of charge at https://pubs.acs.org/doi/10.1021/acs.langmuir.5c05519.

Additional information about DVS models, SANS fitting models, and additional results from SANS fitting (PDF)

## AUTHOR INFORMATION


### Corresponding Authors

**Riccardo Biella** − *Aerospace Structures and Materials Department, Faculty of Aerospace Engineering, Delft University of Technology, Delft 2629 HS, Netherlands;* orcid.org/0009-0007-6575-1285; Email: r.biella@tudelft.nl

**Santiago J. Garcia** − *Aerospace Structures and Materials Department, Faculty of Aerospace Engineering, Delft University of Technology, Delft 2629 HS, Netherlands;* orcid.org/0000-0002-2211-9972; Email: S.J.GarciaEspallargas@tudelft.nl

### Authors

**Lakshmi Satish Nair** − *Aerospace Structures and Materials Department, Faculty of Aerospace Engineering, Delft University of Technology, Delft 2629 HS, Netherlands*

**Steven R. Parnell** − *ISIS Neutron and Muon Source, Rutherford Appleton Laboratory, Didcot OX11 0QX, U.K.; Department of Radiation Science and Technology, Faculty of Applied Sciences, Delft University of Technology, Delft 2629 JB, Netherlands*

**A. Catarina C. Esteves** − *Laboratory of Physical Chemistry, Department of Chemical Engineering and Chemistry, Eindhoven University of Technology, Eindhoven 5600 MB, Netherlands;* orcid.org/0000-0001-7614-5108

**Chintankumar Patel** − *BASF SE, Ludwigshafen am Rhein 67056, Germany*

**Patrick Keil** − *BASF Coatings GmbH, Muenster 48165, Germany;* orcid.org/0000-0001-7899-0882

Complete contact information is available at: https://pubs.acs.org/10.1021/acs.langmuir.5c05519


### Notes

The authors declare no competing financial interest.

## ACKNOWLEDGMENTS

The authors would like to acknowledge BASF SE, BASF Coatings GmbH, and Holland High Tech program for the financial support and useful discussions. The authors would also like to thank Zamran Zahoor Khan for the support at the LARMOR instrument (UK) and Ton Staring for the DVS tests at the TU Eindhoven (NL). The SANS data can be found in the ISIS data repository.[59,60]

## REFERENCES

(1) Keddie, J. L.; Routh, A. F. *Fundamentals of Latex Film Formation*; Springer Laboratory; Springer Netherlands: Dordrecht, 2010

(2) Iannuzzi, M.; Frankel, G. S. The Carbon Footprint of Steel Corrosion. *npj Mater. Degrad.* **2022**, *6*, 101.

(3) Lyon, S. B.; Bingham, R.; Mills, D. J. Advances in Corrosion Protection by Organic Coatings: What We Know and What We Would like to Know. *Prog. Org. Coat.* **2017**, *102*, 2−7.

(4) Philippe, L. V. S.; Lyon, S. B.; Sammon, C.; Yarwood, J. Validation of Electrochemical Impedance Measurements for Water Sorption into Epoxy Coatings Using Gravimetry and Infra-Red Spectroscopy. *Corros. Sci.* **2008**, *50* (3), 887−896.

(5) Allahar, K. N.; Bierwagen, G. P.; Gelling, V. J. Understanding Ac-Dc-Ac Accelerated Test Results. *Corros. Sci.* **2010**, *52* (4), 1106−1114.

(6) Allahar, K. N.; Hinderliter, B. R.; Tallman, D.; Bierwagen, G. Water Transport in Multilayer Organic Coatings. *ECS Trans.* **2008**, *6* (24), 41−55.
(7) Hinderliter, B. R.; Croll, S. G.; Tallman, D. E.; Su, Q.; Bierwagen, G. P. Interpretation of EIS Data from Accelerated Exposure of Coated Metals Based on Modeling of Coating Physical Properties. *Electrochim. Acta* **2006**, *51* (21), 4505−4515.
(8) Stafford, O. A.; Hinderliter, B. R.; Croll, S. G. Electrochemical Impedance Spectroscopy Response of Water Uptake in Organic Coatings by Finite Element Methods. *Electrochim. Acta* **2006**, *52* (3), 1339−1348.
(9) Bongiorno, V.; Michailidou, E.; Curioni, M.; Lyon, S. Unsupervised Classification of Organic Coating Performance Using Electrochemical Impedance Data. *J. Appl. Electrochem.* **2025**, *55*, 1947.
(10) Morsch, S.; Liu, Y.; Lyon, S. B.; Gibbon, S. R. Insights into Epoxy Network Nanostructural Heterogeneity Using AFM-IR. *ACS Appl. Mater. Interfaces* **2016**, *8* (1), 959−966.
(11) Morsch, S.; Emad, S.; Lyon, S. B.; Gibbon, S. R.; Irwin, M. The Location of Adsorbed Water in Pigmented Epoxy-Amine Coatings. *Prog. Org. Coat.* **2022**, *173*, 107223.
(12) Gromer, A.; Thalmann, F.; Hébraud, P.; Holl, Y. Simulation of Vertical Surfactant Distributions in Drying Latex Films. *Langmuir* **2017**, *33* (2), 561−572.
(13) Arnold, C.; Thalmann, F.; Marques, C.; Marie, P.; Holl, Y. Surfactant Distribution in Waterborne Acrylic Films. 1. Bulk Investigation. *J. Phys. Chem. B* **2010**, *114* (28), 9135−9147.
(14) Belaroui, F.; Hirn, M. P.; Grohens, Y.; Marie, P.; Holl, Y. Distribution of Water-Soluble and Surface-Active Low-Molecular-Weight Species in Acrylic Latex Films. *J. Colloid Interface Sci.* **2003**, *261* (2), 336−348.
(15) Keddie, J. L.; Meredith, P.; Jones, R. A. L.; Donald, A. M. Kinetics of Film Formation in Acrylic Latices Studied with Multiple-Angle-of-Incidence Ellipsometry and Environmental SEM. *Macromolecules* **1995**, *28*, 2673−2682.
(16) Gonzalez, E.; Tollan, C.; Chuvilin, A.; Barandiaran, M. J.; Paulis, M. Determination of the Coalescence Temperature of Latexes by Environmental Scanning Electron Microscopy. *ACS Appl. Mater. Interfaces* **2012**, *4* (8), 4276−4282.
(17) Van Der Kooij, H. M.; Van De Kerkhof, G. T.; Sprakel, J. A Mechanistic View of Drying Suspension Droplets. *Soft Matter* **2016**, *12* (11), 2858−2867.
(18) Van Der Kooij, H. M.; Fokkink, R.; Van Der Gucht, J.; Sprakel, J. Quantitative Imaging of Heterogeneous Dynamics in Drying and Aging Paints. *Sci. Rep.* **2016**, *6*, 34383.
(19) Gonzalez, E.; Paulis, M.; Barandiaran, M. J.; Keddie, J. L. Use of a Routh-Russel Deformation Map to Achieve Film Formation of a Latex with a High Glass Transition Temperature. *Langmuir* **2013**, *29* (6), 2044−2053.
(20) Juhué, D.; Wang, Y.; Lang, J.; Leung, O.-M.; Goh, M. C.; Winnik, M. A. Surfactant Exudation in the Presence of a Coalescing Aid in Latex Films Studied by Atomic Force Microscopy1. *J. Polym. Sci. B Polym. Phys.* **1995**, *33* (7), 1123−1133.
(21) Lee, D. Y.; Choi, H. Y.; Park, Y. J.; Khew, M. C.; Ho, C. C.; Kim, J. H. Kinetics of Film Formation of Poly(n-Butyl Methacrylate) Latex in the Presence of Poly(Styrene/$\alpha$-Methylstyrene/Acrylic Acid) by Atomic Force Microscopy. *Langmuir* **1999**, *15* (23), 8252−8258.
(22) Shin, J. S.; Lee, D. Y.; Ho, C. C.; Kim, J. H. Effect of Annealing on the Surface Properties of Poly(n-Butyl Methacrylate) Latex Films Containing Poly(Styrene/$\alpha$-Methylstyrene/Acrylic Acid). *Langmuir* **2000**, *16* (4), 1882−1888.
(23) Santos, J. P.; Corpart, P.; Wong, K.; Galembeck, F. Heterogeneity in Styrene-Butadiene Latex Films. *Langmuir* **2004**, *20* (24), 10576−10582.
(24) Hu, S.; Rieger, J.; Roth, S. V.; Gehrke, R.; Leyrer, R. J.; Men, Y. GIUSAXS and AFM Studies on Surface Reconstruction of Latex Thin Films during Thermal Treatment. *Langmuir* **2009**, *25* (7), 4230−4234.
(25) Vagias, A.; Chen, Q.; Ten Brink, G. H.; Hermida-Merino, D.; Scheerder, J.; Portale, G. Investigation of the Nanoscale Morphology in Industrially Relevant Clearcoats of Waterborne Polymer Colloids by Means of Variable-Angle Grazing Incidence Small-Angle X-Ray Scattering. *ACS Appl. Polym. Mater.* **2019**, *1* (9), 2482−2494.
(26) Konko, I.; Guriyanova, S.; Boyko, V.; Sun, L.; Liu, D.; Reck, B.; Men, Y. Role of the Hydrophilic Latex Particle Surface in Water Diffusion into Films from Waterborne Polymer Colloids. *Langmuir* **2019**, *35* (18), 6075−6088.
(27) Keslarek, A. J.; Rodrigues Costa, C. A.; Galembeck, F. Electric Charge Clustering and Migration in Latex Films: A Study by Scanning Electric Potential Microscopy. *Langmuir* **2001**, *17* (25), 7886−7892.
(28) Pohl, K.; Adams, J.; Johannsmann, D. Correlation between Particle Deformation Kinetics and Polymer Interdiffusion Kinetics in Drying Latex Films. *Langmuir* **2013**, *29* (36), 11317−11321.
(29) Hu, S.; Rieger, J.; Lai, Y.; Roth, S. V.; Gehrke, R.; Men, Y. In-Situ Observation of Drying Process of a Latex Droplet by Synchrotron Small-Angle X-Ray Scattering. *Macromolecules* **2008**, *41* (13), 5073−5076.
(30) Hu, S.; Rieger, J.; Yi, Z.; Zhang, J.; Chen, X.; Roth, S. V.; Gehrke, R.; Men, Y. Structural Evolution of a Colloidal Crystal Fiber during Heating and Annealing Studied by in Situ Synchrotron Small Angle X-Ray Scattering. *Langmuir* **2010**, *26* (16), 13216−13220.
(31) Hammouda, B. Probing Nanoscale Structures-The Sans Toolbox. https://www.eng.uc.edu/~beaucag/Classes/Properties/the_SANS_toolbox.pdf (accessed 2025-12-10).
(32) Polym, C.; Chevalier, Y.; Pichot, C.; Graillat, C.; Joanicot, M.; Wong, K.; Maquet, J.; Lindner, P.; Cabane, B. Film Formation with Latex Particles. *Colloid Polymer Science* **1992**, *270*, 806.
(33) Rharbi, Y.; Boué, F.; Joanicot, M.; Cabane, B. Deformation of Cellular Polymeric Films. *Macromolecules* **1996**, *29* (12), 4346−4359.
(34) Joanicot, M.; Wong, K.; Cabane, B. Interdiffusion in Cellular Latex Films. *Macromolecules* **1996**, *29* (14), 4976−4984.
(35) Joanicot, M.; Granier, V.; Wong, K. Structure of Polymer within the Coating: An Atomic Force Microscopy and Small Angle Neutrons Scattering Study. *Prog. Org. Coat.* **1997**, *32*, 109.
(36) Chevalier, Y.; Hidalgo, M.; Cavaillé, J. Y.; Cabane, B. Structure of Waterborne Organic Composite Coatings. *Macromolecules* **1999**, *32* (23), 7887−7896.
(37) Dingenouts, N.; Ballauff, M. First Stage of Film Formation by Latexes Investigated by Small-Angle x-Ray Scattering. *Langmuir* **1999**, *15* (9), 3283−3288.
(38) Belaroui, F.; Cabane, B.; Dorget, M.; Grohens, Y.; Marie, P.; Holl, Y. Small-Angle Neutron Scattering Study of Particle Coalescence and SDS Desorption during Film Formation from Carboxylated Acrylic Latices. *J. Colloid Interface Sci.* **2003**, *262* (2), 409−417.
(39) van der Wel, G. K.; Adan, O. C. G. Moisture in Organic Coatings—a Review. *Prog. Org. Coat.* **1999**, *37* (1−2), 1−14.
(40) Liu, Y.; Soer, W.-J.; Scheerder, J.; Satgurunathan, G.; Keddie, J. L. Water Vapor Sorption and Diffusion in Secondary Dispersion Barrier Coatings: A Critical Comparison with Emulsion Polymers. *ACS Appl. Mater. Interfaces* **2015**, *7* (22), 12147−12157.
(41) Bakker, S.; Aarts, J.; Esteves, A. C. C.; Metselaar, G. A.; Schenning, A. P. H. J. Water Barrier Properties of Resin-Stabilized Waterborne Coatings for Paperboard. *Macromol. Mater. Eng.* **2022**, *307* (4), 2100829.
(42) Bahaj, H.; Bakass, M.; Bayane, C.; Bellat, J. P.; Benchanaa, M.; Bertrand, G. Modeling of Water Vapor Adsorption Isotherms onto Polyacrylic Polymer. *J. Therm. Anal. Calorim.* **2011**, *103* (1), 117−123.
(43) Brunauer, S.; Deming, L. S.; Deming, W. E.; Teller, E. On a Theory of the van Der Waals Adsorption of Gases. *J. Am. Chem. Soc.* **1940**, *62* (7), 1723−1732.
(44) Favre, E.; Schaetzel, P.; Nguygen, Q. T.; Clément, R.; Néel, J. Sorption, Diffusion and Vapor Permeation of Various Penetrants through Dense Poly(Dimethylsiloxane) Membranes: A Transport Analysis. *J. Membr. Sci.* **1994**, *92* (2), 169−184.
(45) Perrin, L.; Nguyen, Q. T.; Sacco, D.; Lochon, P. Experimental Studies and Modelling of Sorption and Diffusion of Water and Alcohols in Cellulose Acetate. *Polym. Int.* **1997**, *42* (1), 9−16.
(46) Brunel, F.; Galanopoulo, P.; Espinosa Rodriguez, E.; Lansalot, M.; D'Agosto, F. *In Situ* SAXS Investigation of Vinyl Acetate

Polymerization-Induced Self-Assembly. *Polym. Chem.* **2024**, *15* (10), 979−990.
(47) Matsuoka, H.; Tanaka, H.; Hashimoto, T.; Ise, N. Elastic Scattering from Cubic Lattice Systems with Paracrystalline Distortion. *Phys. Rev. B:Condens. Matter Mater. Phys.* **1987**, *36* (3), 1754−1765.
(48) Wong, K.; Richard, J.; Cabanes Rhdne-Poulenc, B.; mixte CEA-RP, E. Ripening of Cellular Latex Filmŝ. *Macromolecules* **1993**, *26*, 3168.
(49) Hammouda, B. A New Guinier−Porod Model. *J. Appl. Crystallogr.* **2010**, *43* (4), 716−719.
(50) González, E.; Paulis, M.; Barandiaran, M. J. Effect of Controlled Length Acrylic Acid-Based Electrosteric Stabilizers on Latex Film Properties. *Eur. Polym. J.* **2014**, *59*, 122−128.
(51) González, E.; Barandiaran, M. J.; Paulis, M. Isolation of the Effect of the Hairy Layer Length on the Mechanical Properties of Waterborne Coatings. *Prog. Org. Coat.* **2015**, *88*, 137−143.
(52) Haley, J. C.; Liu, Y.; Winnik, M. A.; Lau, W. The Onset of Polymer Diffusion in a Drying Acrylate Latex: How Water Initially Retards Coalescence but Ultimately Enhances Diffusion. *J. Coat. Technol. Res.* **2008**, *5* (2), 157−168.
(53) Kureha, T.; Hiroshige, S.; Suzuki, D.; Sawada, J.; Aoki, D.; Takata, T.; Shibayama, M. Quantification for the Mixing of Polymers on Microspheres in Waterborne Latex Films. *Langmuir* **2020**, *36* (18), 4855−4862.
(54) Cramer, S. E.; Bauer, C.; Jeschke, G.; Spiess, H. W. High-Field EPR Studies on Polymer Film Formation from Colloidal Dispersions. *Applied Magnetic Resonance* **2001**, *21*, 495.
(55) Martín-Fabiani, I.; Makepeace, D. K.; Richardson, P. G.; Lesage De La Haye, J.; Venero, D. A.; Rogers, S. E.; D'Agosto, F.; Lansalot, M.; Keddie, J. L. In Situ Monitoring of Latex Film Formation by Small-Angle Neutron Scattering: Evolving Distributions of Hydrophilic Stabilizers in Drying Colloidal Films. *Langmuir* **2019**, *35* (10), 3822−3831.
(56) Klein, G.; Le Houérou, V.; Gauthier, C.; Holl, Y. Friction Properties of Acrylic-Carboxylated Latex Films. 2: Effect of Post Added Surfactant. *Tribol. Int.* **2013**, *57*, 257−265.
(57) Routh, A. F.; Russel, W. B. Process Model for Latex Film Formation: Limiting Regimes for Individual Driving Forces. *Langmuir* **1999**, *15* (22), 7762−7773.
(58) Routh, A. F.; Russel, W. B. Deformation Mechanisms during Latex Film Formation: Experimental Evidence. *Ind. Eng. Chem. Res.* **2001**, *40* (20), 4302−4308.
(59) Biella, R. *Correlating the Surfactant-Rich Interparticle Volume to the Water Absorption and Rheological Behaviour in a Model Waterborne Coating*; STFC ISIS Neutron and Muon Source, 2025
(60) Biella, R. *Correlating the Surfactant-Rich Interparticle Volume to the Water Absorption and Rheological Behaviour in a Model Waterborne Coating*; STFC ISIS Neutron and Muon Source, 2024




https://doi.org/10.1021/acs.langmuir.5c05519
*Langmuir* 2026, 42, 10205−10222